2
Modeling and Simulation of Micro Reactors

2.1
Introduction

In the field of conventional, macroscopic process technology, modeling and simulation approaches are now used on a routine basis to design and optimize processes and equipment. Many of the models employed have been developed for and carefully adjusted to specific processes and reactors and allow one to predict flow as well as heat and mass transfer, sometimes with a high degree of accuracy. In comparison, modeling and simulation approaches for micro reactors are more immature, but bear great potential for even more reliable computer-based process engineering, as will be discussed below. In general, the purposes of computer simulations are manifold, such as feasibility studies, optimization of process equipment, failure modeling or modeling of process data. For each of these tasks within the field of chemical engineering, simulation methods have been applied successfully in the last few years.

Micro reactors are developed for a variety of different purposes, specifically for applications which require high heat and mass transfer coefficients and well-defined flow patterns. The spectrum of applications includes gas and liquid flow as well as gas/liquid or liquid/liquid multi-phase flow. The variety and complexity of flow phenomena clearly pose major challenges to the modeling approaches, especially when additional effects such as mass transfer and chemical kinetics have to be taken into account. However, there is one aspect which makes the modeling of micro reactors in some sense much simpler than that of macroscopic equipment: the laminarity of the flow. Typically, in macroscopic reactors the conditions are such that a turbulent flow pattern develops, thus making the use of turbulence models [1] necessary. With turbulence models the stochastic velocity fluctuations below the scale of grid resolution are accounted for in an effective manner, without the need to model explicitly the time evolution of these fine details of the flow field. Heat and mass transfer processes strongly depend on the turbulent velocity fluctuations, and for this reason the accuracy of the turbulence model is of paramount importance for a reliable prediction of reactor performance. However, there is no model available which is capable of describing turbulent flow phenomena in a universal manner and is computationally inexpensive at the same time. For this reason, simulation approaches for micro reactors, while usually not necessitating

Chemical Micro Process Engineering: Fundamentals, Modelling and Reactions
Volker Hessel, Steffen Hardt, Holger Löwe

ISBN: 3-527-30741-9

turbulence models, offer some potential to make predictions with a degree of accuracy unparalleled by models of macroscopic reactors.

When comparing processes in micro reactors with those in conventional systems, a few general differences can be identified:

- Flow in microstructures is usually laminar (as mentioned above), in contrast to the turbulent flow patterns on the macro scale.
- The diffusion paths for heat and mass transfer are very small, making micro reactors ideal candidates for heat or mass transfer-limited reactions.
- The surface-to-volume ratio of microstructures is very high. Hence surface effects are likely to dominate over volumetric effects.
- The share of solid wall material is typically much higher than in macroscopic equipment. Hence solid heat transfer plays an important role and has to be accounted for when designing micro reactors.

Although the absence of turbulence simplifies many modeling tasks, the predominance of surface effects introduces additional complications, especially in the case of multi-phase flow. Some of the fundamental mechanisms of, e.g., dynamic wetting and spreading phenomena are not yet well understood, thus adding some degree of uncertainty to the modeling of these processes. As more and more practical applications of micro fluidic systems emerge, research in the field of fluidic surface and interfacial phenomena receives additional impetus. It is thus hoped that in the coming years refined models for microfluidic multi-phase systems will be formulated and will add an additional degree of predictability to flow phenomena in micro reactors.

The purpose of this book is to give an overview of reactions, micro reactor designs and simulation methods generic to chemical micro process technology. Although, on the one hand, such a thematic area is delimited from conventional process technology, on the other hand there exists a borderline to the fields of Lab-on-a-Chip (Lab-Chip) and micro total analysis (μTAS) systems. Both Lab-Chip and chemical micro process technology utilize microfluidics, in the one case in order to implement bioanalytical assays and in the other for chemical production. However, there are a couple of differences as far as the principles of microfluidics generic for each application area are concerned. As an example, in chemical micro process technology gas flows are of major importance, whereas Lab-Chip technology is mainly concerned with liquid micro flows. Another example relates to electrokinetic flows, which are rarely used in micro process technology, but have found widespread applications in Lab-Chips. The discussion of micro flow modeling and simulation techniques in the following sections mainly refers to those thematic areas which are of relevance for chemical micro process technology. This means that little attention is paid to some specific topics such as electrokinetic flows, which are almost exclusively related to Lab-Chip and μTAS systems.

2.2
Flow Phenomena on the Micro Scale

When facing the task of formulating a model of a specific microfluidic system, the question arises of whether the conventional macroscopic equations describing fluid flow, heat and mass transfer are still valid on the micro scale. Systems for chemical processing rarely contain structures with dimensions less than 10 µm; the relevant length scale is often in the range of 100 µm. The purpose of this section is to identify the boundaries beyond which the macroscopic description ceases to be valid, in terms of length scales and fluid properties. It will turn out that in many cases the usual macroscopic descriptions can be applied and that genuine micro scale effects mainly appear in gas-phase systems, whereas for many practical applications liquids in micro channels can be described by the usual continuum models. The case of multi-phase systems with free-surface flow requires some special discussion. It should be pointed out that fluid mechanics on the micro scale is a research field of its own. The following sections can only give an overview of the most important effects and provide a general framework for the formulation of models. More detailed discussions can be found elsewhere [2, 3].

2.2.1
Gas Flows

A standard approach to modeling transport phenomena in the field of chemical engineering is based on convection–diffusion equations. Equations of that type describe the transport of a certain field quantity, for example momentum or enthalpy, as the sum of a convective and a diffusive term. A well-known example is the Navier–Stokes equation, which in the case of compressible media is given as

$$\rho\left(\frac{\partial u_i}{\partial t}+u_j\frac{\partial u_i}{\partial x_j}\right)=-\frac{\partial p}{\partial x_i}+\rho\, g_i+\frac{\partial}{\partial x_k}\left[\mu\left(\frac{\partial u_i}{\partial x_k}+\frac{\partial u_k}{\partial x_i}-\frac{2}{3}\delta_{ik}\frac{\partial u_j}{\partial x_j}\right)\right], \qquad (1)$$

where u_i denotes the ith component of the fluid velocity, ρ and μ density and dynamic viscosity, p pressure, g_i the ith component of the gravity vector and δ_{ij} the Kronecker symbol. Derivatives are taken with respect to space and time coordinates and the Einstein convention of summation over repeated indices is assumed throughout this book. Summation indices always appear as lower-case letters i, j, k, l, m and n, if not explicitly stated otherwise. The Navier–Stokes equation can be viewed as a transport equation for the momentum of the fluid. There are two different mechanisms for momentum transport. The first mechanism, convection, is modeled by the last term on the left-hand side of Eq. (1). The convective term describes transport of local fluid momentum along the streamlines of the flow, co-moving with the particles of the fluid. In the co-moving frame of reference, the local momentum density changes either due to a pressure difference (first term on the right-hand side), gravitational forces (second term) or viscous dissipation (last term). The dissipation term describes diffusive transport of momentum due to thermal motion of the particles.

The Navier–Stokes equation defines a set of three relations for four unknown quantities, u_1, u_2, u_3 and p. Another equation is needed to close the set, which is the equation of mass conservation:

$$\frac{\partial \rho}{\partial t} + \frac{\partial}{\partial x_i}(\rho\, u_i) = 0\,. \tag{2}$$

Similar convection–diffusion equations to the Navier–Stokes equation can be formulated for enthalpy or species concentration. In all of these formulations there is always a superposition of diffusive and convective transport of a field quantity, supplemented by source terms describing creation or destruction of the transported quantity. There are two fundamental assumptions on which the Navier–Stokes and other convection–diffusion equations are based. The first and most fundamental is the continuum hypothesis: it is assumed that the fluid can be described by a scalar or vector field, such as density or velocity. In fact, the field quantities have to be regarded as local averages over a large number of particles contained in a volume element embracing the point of interest. The second hypothesis relates to the local statistical distribution of the particles in phase space: the standard convection–diffusion equations rely on the assumption of local thermal equilibrium. For gas flow, this means that a Maxwell–Boltzmann distribution is assumed for the velocity of the particles in the frame-of-reference co-moving with the fluid. Especially the second assumption may break down when gas flow at high temperature or low pressure in micro channels is considered, as will be discussed below.

The principle quantity determining the flow regime of gases and deviations from the standard continuum description is the Knudsen number, defined as

$$\mathrm{Kn} = \frac{\lambda}{L}\,. \tag{3}$$

Kn is the ratio of two length scales, the mean free path of the gas molecules λ and a characteristic length scale of the flow domain L, for example the channel diameter. For molecules interacting as hard spheres of diameter d, the mean free path is given as (see, e.g., [4])

$$\lambda = \frac{k_\mathrm{B}\, T}{\sqrt{2}\,\pi\, p\, d^2}\,, \tag{4}$$

where k_B is the Boltzmann constant, T, p are temperature and pressure and d is the hard-sphere diameter. When Kn > 1, a gas molecule is more likely to collide with the channel wall than with another molecule. As the transport of momentum or enthalpy is to a large extent governed by the collisions between molecules, major changes in the flow behavior are expected when the Knudsen number exceeds 1. This may happen when gas flow through narrow channels is considered, but also when the temperature is high and/or the pressure is low.

Based on the Knudsen number, four different flow regimes can be distinguished [5]:

- continuum flow with no-slip boundary conditions ($Kn \leq 10^{-2}$);
- continuum flow with slip boundary conditions ($10^{-2} < Kn \leq 10^{-1}$);
- transition flow ($10^{-1} < Kn \leq 10$);
- free molecular flow ($Kn > 10$).

In the first two cases the Navier–Stokes equation can be applied, in the second case with modified boundary conditions. The computationally most difficult case is the transition flow regime, which, however, might be encountered in micro-reactor systems. Clearly, the defined ranges of Knudsen numbers are not rigid; rather they vary from case to case. However, the numbers given above are guidelines applicable to many situations encountered in practice.

2.2.1.1 Slip Flow Regime

For applications in the field of micro reaction engineering, the conclusion may be drawn that the Navier–Stokes equation and other continuum models are valid in many cases, as Knudsen numbers greater than 10^{-1} are rarely obtained. However, it might be necessary to use slip boundary conditions. The first theoretical investigations on slip flow of gases were carried out in the 19th century by Maxwell and von Smoluchowski. The basic concept relies on a so-called slip length L_s, which relates the local shear strain to the relative flow velocity at the wall:

$$u_{gas} - u_{wall} = L_s \frac{\partial u_{gas}}{\partial y} \Bigg|_{Wall} . \tag{5}$$

For this purpose a coordinate frame is introduced with the x-coordinate in the flow direction and the y-coordinate perpendicular to the wall (see Figure 2.1). For isothermal conditions the above relation was rigorously derived by Maxwell from the kinetic theory of monoatomic gases. The slip length enters as an empirical parameter containing information on how the gas molecules interact with the wall. There are two limiting cases for this interaction. In the first case, called 'specular reflection', the tangential velocity component of a molecule is conserved and the normal component is inverted. Thus, the momentum transfer of the molecule to the wall in flow direction vanishes. Such an interaction can be imagined to occur when the walls are 'smooth'. In the case of a more intense interaction, or synonymously 'rough' walls, the molecule can transfer longitudinal momentum to the walls. The limiting case where the molecule has lost the 'memory' on its velocity before the collision with the wall and is reflected randomly to all angles is called 'diffuse reflection'. The two limiting cases are illustrated in Figure 2.1.

When the fractions of molecules reflected specularly and diffusively are known, the slip length can be determined, as shown by Maxwell. Maxwell introduced a tangential momentum accommodation coefficient defined as

$$\sigma_v = \frac{\tau_i - \tau_r}{\tau_i - \tau_w} , \tag{6}$$

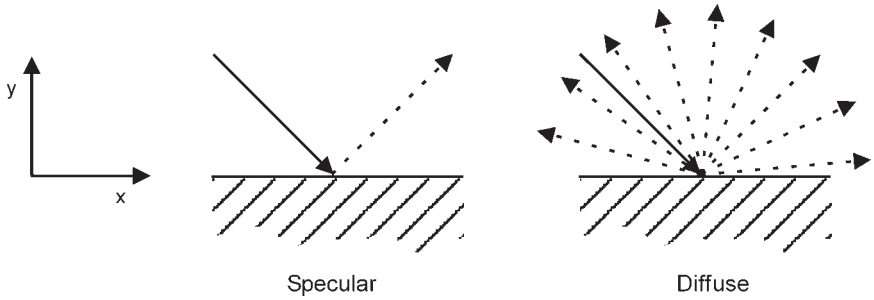

Figure 2.1 Velocity vectors of a gas molecule for specular (left) and diffuse (right) reflection.

where τ_i denotes the average tangential momentum of the incoming molecules, τ_r that of the reflected molecules and τ_w the tangential momentum of a molecule co-moving with the wall. In the case of specular reflection, σ_v assumes a value of zero. Based on the accommodation coefficient, the slip length is given by

$$L_s = \frac{2 - \sigma_v}{\sigma_v} \lambda \,. \tag{7}$$

Apparently, the slip length diverges when $\sigma_v \to 0$. In practice, the shear strain in Eq. (5) will approach zero in such a case, thus leaving the velocity jump finite. Several experimental results on σ_v have been reported [6, 7], most of them indicating values between 0.8 and 1.0, compatible with 'rough' walls.

The physical reason for the velocity slip is the fact that close to the wall the gas is not in thermal equilibrium. For the same reason, a temperature jump is induced, and a more detailed investigation based on the kinetic theory of gases shows that heat transfer and momentum transfer are coupled. Expressions for velocity slip and temperature jump valid in the case of non-isothermal conditions are given by

$$u_{gas} - u_{wall} = \frac{2 - \sigma_v}{\sigma_v} \lambda \frac{\partial u_{gas}}{\partial y} + \frac{3}{4} \frac{\mu}{\rho T_{gas}} \frac{\partial T_{gas}}{\partial x} \,, \tag{8}$$

$$T_{gas} - T_{wall} = \frac{2 - \sigma_T}{\sigma_T} \frac{2\gamma}{\gamma + 1} \frac{\lambda}{\mathrm{Pr}} \frac{\partial T_{gas}}{\partial y} \,. \tag{9}$$

All derivatives are to be evaluated at the wall. In these expressions, μ and ρ are the viscosity and density of the gas, γ is the ratio of specific heats of the gas and the wall material and the Prandtl number of the gas is defined as

$$\mathrm{Pr} = \frac{c_p \mu}{k} \,, \tag{10}$$

with the specific heat c_p and the thermal conductivity k. The thermal accommodation coefficient σ_T is defined similarly to the tangential momentum accommo-

dation coefficient. An interesting effect which can be derived from the second term on the right-hand side of Eq. (8) is *thermal creep*. In a microfluidic channel, an axial heat flux through the wall material induces a flow in the opposite direction.

Relations as those defined by Eqs. (8) and (9) can be viewed as a special case of a low-Knudsen number expansion which in case of isothermal conditions is given as [8]

$$u_{\text{gas}} - u_{\text{wall}} = \frac{2-\sigma_{\text{v}}}{\sigma_{\text{v}}}\left(\text{Kn}\,\frac{\partial u_{\text{gas}}}{\partial n} + \frac{\text{Kn}^2}{2}\,\frac{\partial^2 u_{\text{gas}}}{\partial n^2} + \ldots\right), \tag{11}$$

where n denotes a unit vector normal to the wall. As will be discussed below, the Navier–Stokes equation can be obtained from an expansion of the Boltzmann equation up to first order in Kn. Although higher-order expansions of the flow boundary conditions as indicated in Eq. (11) are more accurate in the slip-flow and the transition-flow regime, using such boundary conditions is of little use in combination with the Navier–Stokes equation which is of lower order accuracy.

2.2.1.2 Transition Flow and Free Molecular Flow

In the transition flow and free molecular regime, the use of the Navier–Stokes equation with slip-flow boundary conditions is no longer justified. A general framework for computing gas flows at arbitrary rarefaction is provided by the Boltzmann equation. One might argue that the transition flow regime is rarely reached in micro reactors. However, the first microfluidic systems with sub-micron structures have already been reported, although for liquid-flow applications [9–12]. As nanotechnology becomes more mature, more applications in the field of nanofluidics might open up. Apart from of hypothetical future developments, a well-known component of chemical reaction systems requires an understanding of transport processes in the transition of the free molecular regime: porous media. Often, catalyst materials used for heterogeneously catalyzed gas-phase reactions contain pores with diameters in the nanometer range. Such nanoporous materials are beginning to be used in the field of micro process technology [13, 14]. A brief survey of models for transition and free molecular flows is thus justified.

A detailed derivation and discussion of the Boltzmann equation can be found in many standard statistical physics textbooks, for example [15]. The Boltzmann equation is based on a distribution function $f(x_i, u_i, t)$ defined such that $f(x_i, u_i, t)\, d^3r\, d^3u$ represents the average number of molecules in a phase space volume element around (x_i, u_i), i.e. the distribution function is related to the probability of finding a molecule at spatial coordinates x_i with velocity components u_i. For molecules of mass m in an external force field with components $F_i(x_j)$ the equation takes the form

$$\frac{\partial f}{\partial t} + u_i\,\frac{\partial f}{\partial x_i} + \frac{F_i}{m}\,\frac{\partial f}{\partial u_i} = J(f, f^*)\,. \tag{12}$$

The right-hand side of this equation is the so-called collision integral, an integral over terms quadratic in the distribution function (in the case of binary collisions) containing the molecular scattering cross-section. The collision integral describes the rearrangement of the distribution function due to molecular collisions. The terms on the left-hand side describe the collision-less evolution of the molecular distribution due to external forces, for example gravitation. For two reasons the Boltzmann equation is much more difficult to solve than the Navier–Stokes equation. On the one hand, it is an integro-differential equation containing a coupling of points in phase-space separated by a finite distance. On the other hand, the unknown function to be solved for is a function not only of the spatial coordinates, but also of the velocity coordinates.

In order to reduce the complexity of the problem, several approximation schemes have been developed. In the BGK model, the collision integral is replaced by a simple local term ensuring that the well-known Maxwell distribution is reached at thermal equilibrium [16]. The linearization method assumes that the phase space distribution is given by a small perturbation h on top of a (local) Maxwell distribution f_0 (see, e.g., [17, 18]):

$$f(x_i, u_i, t) = f_0[1 + h(x_i, u_i, t)]\,. \tag{13}$$

In order to establish a link with the Navier–Stokes equation, the distribution function can be expanded in a series of powers of the Knudsen number as

$$f = f^{(0)} + \mathrm{Kn}\, f^{(1)} + \mathrm{Kn}^2\, f^{(2)} + \ldots\,. \tag{14}$$

When this so-called Chapman–Enskog expansion [19] is inserted into the Boltzmann equation, a series of equations of different approximation order in Kn is obtained. To lowest order, the Euler equation, i.e. the Navier–Stokes equation in the limit of vanishing viscosity, is recovered. The next approximation level yields the Navier–Stokes equation, in the second-order approximation a generalization of the Navier–Stokes equation is obtained, the so-called Burnett equations. The Burnett equations could be employed to describe gas flows in the transition regime; they are, however, rarely used in practice, owing to their complexity and uncertainties related to the implementation of boundary conditions. The standard approach for computing transition flows is the direct simulation Monte Carlo (DSMC) method, which will be outlined below. In addition, approaches aiming at solving the Boltzmann equation directly, partially making use of approximations as in the BGK model, are used to describe transition flows [20].

In order to obtain a qualitative view of how the transition regime differs from the continuum flow or the slip flow regime, it is instructive to consider a system close to thermodynamic equilibrium. In such a system, small deviations from the equilibrium state, described by thermodynamic forces X_i, cause thermodynamic fluxes J_i which are linear functions of the X_i (see, e.g., [15]):

$$J_\mathrm{i} = \sum_j \Lambda_\mathrm{ij}\, X_\mathrm{j} \tag{15}$$

As an example, J_i can be a heat flux and X_i a temperature gradient. The thermodynamic fluxes determine the irreversible time evolution of a system to thermodynamic equilibrium, e.g. a temperature difference can be equalized by a heat flux. In general, the kinetic coefficients Λ_{ij} are non-zero for $i \neq j$, implying several so-called cross-diffusion effects. As an example, a concentration gradient can induce a heat flux or a temperature gradient a mass flow. The coupling between the velocity field and the temperature field of Eq. (8) is a special case of mass flow being induced by a temperature gradient. When rarefaction effects are absent, the non-diagonal terms of the kinetic-coefficients matrix can be neglected in many cases. This is no longer true in the transition flow regime, where cross-diffusion effects become equally important as the diagonal contributions to Eq. (15) [21]. In the transition flow regime, gradients of field quantities such as temperature and concentration induce fluxes of other quantities to which they are linked by the kinetic coefficients to a similar extent as observed for the self-induced fluxes. Thus, the coupling between different field quantities becomes much stronger than in the continuum flow regime.

Nowadays, the DSMC method has become the standard approach for simulation of gas flows in the transition regime [4]. Rather than modeling gas flow by a set of differential or integro-differential equations, this method is based on tracking the trajectories and interactions of gas molecules directly. DSMC is a time marching approach based on a time discretization with steps smaller than the collision time of the molecules. The computational domain is divided into cells with a size smaller than the molecular mean free path. Particles are initialized inside the computational domain. In one time step, a particle moves along its velocity vector, potentially penetrating into a neighboring cell. Inside each cell, the particles can undergo collisions with other particles, changing their velocity vectors. In a sense, DSMC attempts to model the physical scenario of molecular motion interrupted by collisions with other molecules directly. However, even in small systems of a few microns extension, the number of gas molecules is tremendously high. A modeling approach following the trajectories of all of these molecules would typically require computational resources exceeding the capabilities of most of today's computers. For this reason, each particle in a DSMC simulation represents a whole ensemble of molecules. Specifically, a DSMC algorithm comprises a repeated sequence of the following steps:

- *Particle motion*
  Particles are moved along their current velocity vectors without undergoing interactions for a time Δt which is chosen smaller than the mean collision time. If a particle hits the domain boundary, its velocity vector is modified according to the corresponding boundary condition (for example specular or diffuse reflection if a particle hits a wall);

- *Indexing and tracking of particles*
  Attached to each particle is information on the computational cell in which it is located. During a time step a particle might enter a neighboring cell. It is then necessary to update the cell index of the particle.

- *Collision of particles*
  Based on the molecular collision cross-section, a particle might undergo a collision with another particle in the same cell. In a probabilistic process collision partners are determined and velocity vectors are updated according to the collision cross-section. Typically, simple parametrizations of the cross-section such as the hard-sphere model for monoatomic gases are used.

- *Sampling of macroscopic quantities*
  Macroscopic quantities of interest such as pressure, density or average velocity are obtained by sampling over the particle distribution within each cell. Usually sampling from only one simulation run is not sufficient to obtain quantities with an acceptable noise level; instead results are obtained by averaging over many parallel runs.

DSMC simulations have been employed to study flow in micro channels [22–24]. The number of simulated particles usually lies in the range of several hundred thousand to several million. Despite this apparently high number, there still exist considerable problems with statistical noise. For the specific application of micro channel flows, it is very difficult to extract reliable velocity profiles at low Mach numbers. The reason for these problems lies in the different velocity scales of the flow and the single molecules. For low-speed flows the molecular velocity exceeds the flow velocity by orders of magnitude, thus making the extraction of a small non-zero average from a largely fluctuating ensemble very difficult. By the statistical nature of the DSMC approach, the errors are inversely proportional to the square root of the number of simulated molecules. Hence an increase of the number of molecules effects only a slight reduction in the statistical errors. The simulation of low-speed flows by DSMC is a field of ongoing research. A special DSMC scheme has been developed where the particles carry information not only on their microscopic velocity but also on the velocity of a macroscopic ensemble represented by the particle [23, 25]. Alternatively, non-linear filters have been used for post-processing DSMC results and extracting macroscopic quantities from a noisy ensemble [24]. Such novel approaches help to reduce the noise level considerably and allow one to obtain more reliable results for low-speed flows.

In Figure 2.2 DSMC results of Karniadakis and Beskok [2] and results obtained with the linearized Boltzmann equation are compared for channel flow in the transition regime. The velocity profiles at two different Knudsen numbers are shown. Apparently, the two results match very well. The fact that the velocity does not reach a zero value at the channel walls ($Y = 0$ and $Y = 1$) indicates the velocity slip due to rarefaction which increases at higher Knudsen numbers.

When the channel diameter becomes very small, it might no longer be justified to assume smooth channel walls since, depending on the microfabrication technology used, the surface roughness cannot be neglected on the length scale of the channel diameter. One of the first studies of rarified gas flows in channels with rough surfaces based on the DSMC method was performed by Sun and Faghri [26]. They set up a model geometry of a channel with step structures on its surface, as

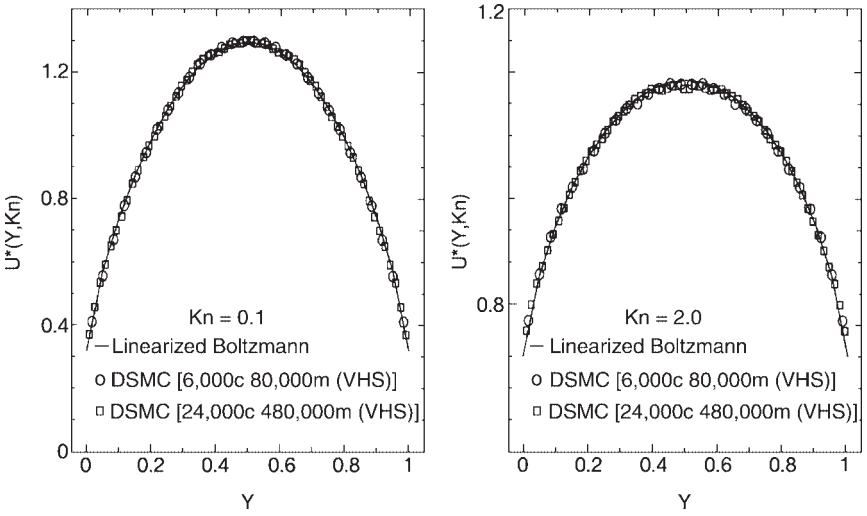

Figure 2.2 Non-dimensionalized velocity distribution across a channel for Kn = 0.1 (left) and Kn = 2.0 (right), taken from [2]. The results were obtained by DSCM using two different collision cross-sections and by solution of the linearized Boltzmann equation.

depicted in Figure 2.3. The model geometry is described by three parameters D_h, s and ε, where the ratio ε/D_h controls the magnitude of the surface roughness. The DSMC simulations were performed for Knudsen numbers between 0.02 and 0.08 and the results were expressed as a friction factor depending on the Knudsen number and the geometry parameters. For very small values of ε/D_h, the friction factor of a smooth channel obtained from continuum theory with slip flow boundary conditions is reproduced. A deviation from the smooth channel results occurs at $\varepsilon/D_h = 5\%$, where the friction factor starts to increase owing to the effects of surface roughness. When varying the Knudsen number it is found that the surface roughness has a larger effect on low Kn flows compared with flows at high Kn.

Owing to the computational cost of the DSMC method, it is advisable to use continuum approaches such as the Navier–Stokes equation wherever possible. In many conceivable situations, there are regions inside of the flow domain where the use of slip boundary conditions in combination with the Navier–Stokes equation is justified, whereas other regions require the use of the DSMC method. A simple example is given by a narrow channel with a high pressure drop. At the entrance of the channel, the pressure and the density are high and the molecular mean free path is comparatively small. As the pressure decreases towards the exit of the channel, the mean-free path increases and the Knudsen number might reach values in the transition regime. An optimized method for such problems would be based on a subdivision of the flow domain into a continuum flow and a transition flow region and would consist of a Navier–Stokes or Euler solver coupled with a DSMC solver. These methods have been developed in the last few years [27, 28] and enhance the applicability of DSMC approaches.

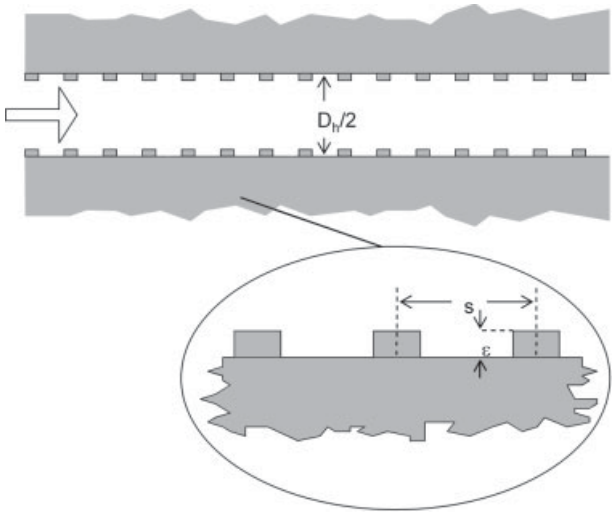

Figure 2.3 Model geometry used for the study of surface-roughness effects on rarefied gas flows in micro channels.

2.2.2 Liquid Flows

The Navier–Stokes equation [Eq. (1)] provides a framework for the description of both liquid and gas flows. Unlike gases, liquids are incompressible to a good approximation. For incompressible flow, i.e. a constant density ρ, the Navier–Stokes equation and the corresponding mass conservation equation simplify to

$$\frac{\partial u_i}{\partial t} + u_j \frac{\partial u_i}{\partial x_j} = -\frac{1}{\rho}\frac{\partial p}{\partial x_i} + g_i + \frac{1}{\rho}\frac{\partial}{\partial x_j}\left(\mu \frac{\partial}{\partial x_j} u_i\right), \tag{16}$$

$$\frac{\partial u_i}{\partial x_i} = 0\,. \tag{17}$$

In some microfluidic applications liquid is transported with a comparatively low velocity. In such cases, a liquid volume co-moving with the flow experiences inertial forces which are small compared with the viscous forces acting on it. The terms appearing on the left-hand side of Eq. (16) can then be neglected and the *creeping flow* approximation is valid

$$\frac{\partial}{\partial x_j}\left(\mu \frac{\partial}{\partial x_j} u_i\right) - \frac{\partial p}{\partial x_i} + \rho\, g_i = 0\,. \tag{18}$$

An indicator of the validity of the creeping flow approximation is the dimensionless Reynolds number:

$$\mathrm{Re} = \frac{u\, d\, \rho}{\mu}, \tag{19}$$

where d is a length scale characteristic for the flow under consideration. The Reynolds number reflects the ratio of inertial and viscous forces and is possibly the most important dimensionless group used to characterize flow fields. It should be small for the creeping flow approximation to be applicable [29]. Eq. (18) is much simpler to solve than the full Navier–Stokes equation, as it is linear in the velocity. As a special scheme suited for such types of problems, the boundary element method allows one to reformulate a fluid dynamics problem in the creeping flow regime for a specific flow domain as a problem defined on its boundary [30] and permits a fast and efficient solution of Eq. (18) in many cases. Hence, whenever attempting to solve a micro flow problem, it is useful to check the validity of the creeping flow approximation.

Similarly to the case of gas flows discussed above, the question of the range of applicability of continuum models for liquid flow arises. While the kinetic theory of gases provides clear indications of the limits of continuum models and of the onset of rarefaction effects on the micro scale, there is no general framework explaining possible deviations of liquid flow phenomena from their macroscopic behavior. The concept of mean free path ceases to be useful for liquids, as the molecules interact with their neighbors in a permanent manner (in a sense, the molecular mean free path is zero for liquids). A few groups have conducted experiments on liquid flows in microstructures and measured pressure drop and heat transfer coefficients, with largely contradictory results. Pfahler et al. [31] measured the pressure drop in channels with depths ranging from 0.5 to 50 μm and found indications for a reduced viscosity. Peng et al. [32] studied liquid flow through rectangular micro channels of hydraulic diameters between 133 and 367 μm. They found that the transition from laminar to turbulent flow occurred at smaller Reynolds numbers than in macroscopic set-ups and increased or reduced friction factors, depending on the aspect ratio of the channel. The same group studied the heat transfer characteristics in micro channels and again found indications of a transition to turbulent flow at smaller Reynolds numbers than in conventional situations [33]. Other groups measured friction factors in good agreement with predictions of the classical theory [34, 35] or higher friction factors than in conventional set-ups [36, 37]. A compilation of the published results does not seem to leave room for any simple conclusions of general importance. Furthermore, the physics of Newtonian liquids does not suggest any universal mechanisms by which the flow behavior in channels of several hundred microns width could differ considerably from macroscopic behavior at the same Reynolds number. However, in some specific situations liquid micro flows exhibit a behavior which does not occur on the macro scale, but which can be reproduced experimentally and explained by theoretical models. A brief overview of such effects is given in the following.

2.2.2.1 Boundary Slip of Liquids

During the last decade, it was confirmed that not only gases, but also liquids can exhibit boundary slip. For liquids the slip length is defined as the distance behind the interface at which the flow velocity extrapolates to zero [38]. Non-Newtonian liquids such as polymer melts often show very pronounced slip-flow effects, as was discovered by Migler et al. [39]. They used a Couette-flow apparatus and an evanescent wave with a penetration depth of the order of 100 nm to photobleach a small liquid volume in the close vicinity of a solid surface. From the fluorescence-recovery curve of their evanescent wave-induced fluorescence experiment, they could determine the slip length, which was larger than 100 μm in some cases. Measurements of slip flow on hydrophobic surfaces were carried out by Baudry et al. [40]. They used an oscillating microscopic sphere in the vicinity of a planar surface and measured the response force due to the oscillations. The slip length determined in such a way was 38 nm. Recently, it was discovered that not only hydrophobic, but also hydrophilic surfaces exhibit boundary slip. By moving a silica sphere with a radius of 10 μm relative to a flat surface by means of a piezo-driven cantilever beam, the slip flow characteristics of a Newtonian liquid were measured via the drag force exerted on the sphere [41]. By comparison with exact solutions of the Stokes equation, a slip length of up to 20 nm was determined, and the slip length was found to increase with shear rate. Other researchers found values of comparable magnitude [42]. In terms of the values characteristic for some microfluidic systems, the shear rates in these experiments were moderate, reaching 8000 s^{-1} at the maximum. Shear rates in that range are characteristic for flow velocities around 1 m s^{-1} in 100 μm wide channels. Such a comparison indicates that boundary slip of liquids might be of some importance for microfluidic systems, especially when high-speed flows in narrow channels are considered.

For a long time, a unified framework for modeling liquid slip-flow effects such as given by Eq. (5) in case of gases has been missing. In 1997, Thompson and Trojan published a result which might be a major step towards a unified description of wall boundary conditions for liquid flows [43]. Their method was based on molecular dynamics (MD) simulations, an approach which is briefly described below. The MD method is similar to the DSMC approach for gases, i.e. the trajectories of single particles are computed. Unlike in DSMC, the particles never travel freely, but permanently move in a force field generated by the other particles. Thompson and Trojan used a well-established model for the intermolecular and molecule–wall interactions, which relies on a shifted Lennard–Jones potential (the fundamentals of molecular interactions are explained in [44], among others). They showed that the slip length in a nanoscale Couette flow geometry varied as a function of the parameters of their interaction potential. The most efficient momentum transfer, or conversely, the smallest slip length was found when the intermolecular distance of the solid wall material equalled that of the liquid. At a critical shear rate the slip length was found to diverge. The results of all of their simulations can be expressed in the following form:

$$L_s = L_{s0}\left(1 - \frac{\dot{\gamma}}{\dot{\gamma}_c}\right)^{-\frac{1}{2}}, \tag{20}$$

with the shear rate given by $\dot{\gamma} = \partial u/\partial y$, as in Eq. (5). L_s is the slip length, and a reference slip length L_{s0} and a critical shear rate $\dot{\gamma}_c$ enter as parameters. In contrast to Eq. (5), the slip length depends non-linearly on the shear rate. When the shear rate reaches a critical value, the slip length diverges, thus indicating that for high-speed flows in small channels deviations from the macroscopic no-slip boundary conditions might be found even on the micrometer scale. It is hoped that in the coming years more information on characteristic values of the free parameters of Eq. (20) will be collected, thus allowing reliable and accurate predictions of high-speed flows in microstructures. Typical numbers reported so far indicate that the slip length of liquid flows in micro scale geometries is small, but not insignificant.

2.2.2.2 Electric Double Layers

Another interfacial phenomenon which is already present in macroscopic flows, but plays a significant role only on the micro scale, is the formation of electric double layers (EDL) [45]. The first theoretical description of EDL formation in liquids was given by Helmholtz in the 19th century. Many surfaces have the ability to bind ions from the liquid phase. A glass surfaces acquires a negative potential when immersed in water. As a consequence, the liquid phase assumes a net positive charge. The positive ions are attracted to the immobilized negative surface charges by electrostatic forces and stay in the vicinity of the surface. However, the electrostatic attraction is counterbalanced by thermal motion of the ions and a polarization layer, the so-called Debye layer, of finite thickness develops. A sketch of the charge distribution in the vicinity of the solid surface is presented in Figure 2.4. The immobilized negative charges are partly balanced by a layer of positive

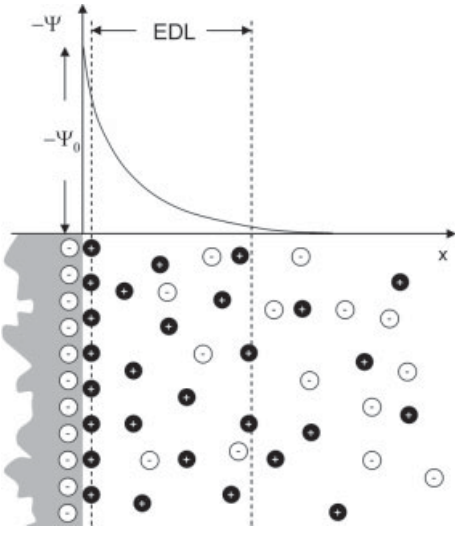

Figure 2.4 Sketch of an electric double layer next to a negatively charged solid surface. Through balance of thermal motion and electrostatic forces a rapidly decaying electric potential Ψ develops inside the liquid phase.

ions sticking to the surface, the so-called Stern layer, followed by an electric double layer of ions dissolved in the liquid. The resulting potential Ψ decays rapidly as a function of distance from the surface.

The EDL charge distribution can be modeled by a Poisson–Boltzmann equation (see, e.g., [46]). In many practical cases values for the layer thickness between 1 and 100 nm are obtained [47].

In comparison, the width of most microfluidic channels is much larger. Hence, whenever EDL effects have to be taken into account in models of microfluidic systems, it is a common strategy to incorporate them as a flow boundary condition rather than resolving the electric double layer explicitly. As a net charge close to the solid surface is created, an external electric field exerts a force on the liquid and can be used to drive a flow. The corresponding transport mechanism is termed *electroosmotic flow* and is used as a fluidic actuation principle in a number of microfluidic systems developed recently [48–50]. The velocity distribution of electroosmotic flow in a capillary has an approximate plug-flow character [51]. This makes electroosmotic flow an interesting principle for microfluidics, as hydrodynamic dispersion are minimized and residence-time broadening and back-mixing is avoided. As mentioned above, in models of electroosmotic flow phenomena the physics of the Debye layer is often incorporated as a flow boundary condition [45]:

$$u_{\mathrm{p}} = -\frac{\zeta\, \varepsilon\, E}{\mu}, \tag{21}$$

where u_{p} is the velocity at the wall, ε is the dielectric constant of the liquid and μ its viscosity. The zeta potential ζ is equal to the potential drop in the electric double layer (i.e. the total potential drop minus the potential drop in the Stern layer) and the flow is driven by an electric field E along the wall. Such an effective implementation of body forces exerted by the electric field avoids resolving the thin electric double layer explicitly and thus helps to limit the computational complexity of a model.

The formation of an electric double layer close to a solid/liquid interface might offer an explanation for micro channel friction factors or heat transfer coefficients deviating from their macroscopic values. Most surfaces carry electric charges, and a net charge is found within the EDL in the mobile liquid phase. When liquid is forced through a micro channel, the molecules drag these charges along with them, thus inducing an electric current. In this way, an electric potential, the so-called streaming potential, builds up between the channel inlet and outlet [52]. On the other hand, the streaming potential induces an electric current against the flow direction, and finally an equilibrium configuration is found where the two currents compensate each other. The drag force due to the current induced by the streaming potential causes an increased friction factor as compared to a situation without EDL. This effect was studied by Yang et al. [53] for rectangular micro channels. They solved the Poisson–Boltzmann and the enthalpy equations with a finite-difference scheme and the Navier–Stokes equation with a Green's function technique. The channel width and height considered was in the range between 20 and 40 μm. Depending on the solute concentration, they found the friction factor to be

significantly increased owing to the presence of an EDL. At the same time, the heat transfer coefficient is reduced by a significant amount. However, the deviations from the corresponding values without EDL rapidly diminish when the channel size increases.

2.2.2.3 Nano Flows

The effects considered above, boundary slip and the formation of electric double layers, are surface effects occurring at the interface of the liquid with a solid. Owing to the large surface-to-volume ratio, they are of potential importance in micro systems but usually negligible in macroscopic systems. Despite these surface effects, the continuum description provided by the Navier–Stokes and other continuum equations remains valid on the micro scale. Only when liquids are confined in nanoscale flow geometries do they show a behavior which can no longer be described with continuum models. Most of the information on nanoflows has been obtained with the help of MD simulations. In the close vicinity of a solid/liquid interface, the liquid molecules usually show a certain ordering which results in density oscillations. Experimental studies of molecular ordering within a few nanometers of a solid surface have been done utilizing the X-ray reflectivity of the molecules [54]. The results of such an experiment are displayed in Figure 2.5. The figure shows the density of oxygen atoms contained in water and exhibits a layer adsorbed to the surface (a) and an ordering of molecules close to the surface (b) which results in density oscillations. Such density oscillations could be reproduced in MD simulation studies [55, 56] and belong to a class of phenomena which are clearly beyond the scope of continuum theories.

Within the MD approach the trajectory of each molecule in the force field generated by the other molecules is computed [57]. For this purpose, Newton's equations of motion are solved:

$$m \frac{\mathrm{d}^2 x_i^{(k)}}{\mathrm{d}t^2} = \sum_{l \neq k} \frac{\partial V_{kl}}{\partial x_i^{(k)}}, \tag{22}$$

where $x_i^{(k)}$ is spatial coordinate i of particle k, V_{kl} is the interaction potential between molecules k and l and m is the molecular mass. In many simulations the Lennard–Jones interaction potential:

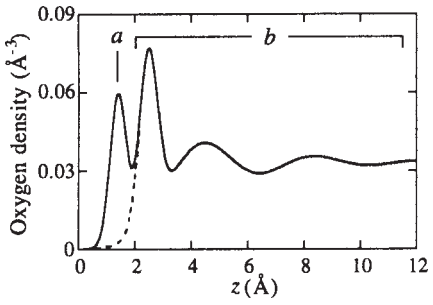

Figure 2.5 Density oscillations of water close to the solid surface, as reported in [54]. The figure shows molecules adsorbed to the surface (a) and in the liquid phase (b).

$$V_{kl}(r) = 4\,\varepsilon\left[\left(\frac{r}{\sigma}\right)^{-12} - \left(\frac{r}{\sigma}\right)^{-6}\right] \tag{23}$$

or slight modifications thereof are used. In this expression, r is the distance between molecules k and l, ε is an energy scale and σ determines the range of the potential. The first term in brackets is a short-range repulsive and the second term a longer range attractive contribution. Potentials of Lennard–Jones type are suited to describe the interaction between neutral, spherical molecules. At the beginning of a simulation, a number of molecules are initialized at specific positions with random velocities sampled from a Maxwell distribution. To compute the time evolution of the system, Eq. (22) is integrated, usually with an explicit, higher order time step algorithm. The integration time steps have to be chosen significantly smaller than the intrinsic time-scale of the problem which is given by

$$\tau = \sqrt{\frac{\sigma^2\, m}{\varepsilon}}\,. \tag{24}$$

The intrinsic time-scale also sets a lower limit to the time the system needs to equilibrate, which is the minimum time the simulation has to run in order to sample average quantities from the molecular ensemble. With no further actions taken, the computational cost of an MD simulation of an ensemble of N molecules is of order $O(N^2)$, as the interactions of each molecule with all other molecules have to be taken into account. However, the Lennard–Jones potential decays as r^{-6}, which means that the contributions of distant molecules can be neglected. This idea has been implemented in algorithms making use of lists of neighboring molecules [58], thereby reducing the computational cost of MD simulations. MD has been used to study laminar channel flow, fluid interfaces and wetting phenomena, among others [57]. Nevertheless, MD simulations remain very challenging. State-of-the-art simulations on high-performance computing platforms are based on numbers of particles in the range of a few billion [59], still not enough for tasks such as following the motion of the $3 \cdot 10^{10}$ water molecules contained in a volume of 1 μm^3.

2.2.3 Multiphase Flows

Several 'unexpected' phenomena have been reported for multiphase systems in milli and micro scale geometries, especially for evaporation of liquids (for an overview, see [60]). Evaporation often occurs via nucleate boiling, and when the bubble size is of the same order of magnitude as the dimension of a fluidic structure, the mechanism of heat removal is modified as compared with, e.g., the classical pool boiling. Viewed from that angle it is not surprising that the conventional correlations for evaporation heat transfer coefficients are not valid in narrow channels or tubes [60]. More difficult to understand are the results of Peng and Wang [61–63], who observed that bubble formation in micro evaporator channels is suppressed,

even though in the manifold behind the channel outlet bubbles were observed, indicating that the process was in the nucleate boiling regime.

In general terms, the phenomena described above belong to the class of phase transitions and critical phenomena in confined spaces. From the field of statistical physics, some far-reaching results applying to such problems are known. One fruitful concept used in statistical physics is the correlation length (see, e.g., [64]). The correlation length describes how a local field quantity evaluated at one point in space is correlated with the same quantity at another point. As an example, the correlation length σ for density fluctuations in a fluid is defined via

$$\left\langle \rho(x_i)\, \rho(x_i + s_i) \right\rangle \propto \exp(-s/\sigma)\,, \tag{25}$$

where ρ is the density, s the magnitude of s_i and $\langle \ldots \rangle$ denotes the thermodynamic average. Naturally, the above definition only refers to systems where correlations decay exponentially as a function of distance. When a thermodynamic system approaches the critical temperature T_c for a phase transition, the correlation length diverges with a critical exponent ν [65]:

$$\sigma \propto | T - T_c |^{-\nu}\,. \tag{26}$$

Hence, close to the critical point thermodynamic quantities at comparatively distant spatial locations become correlated. Especially in the case of liquid micro flows close to a phase transition, these considerations suggest that the correlation length and not the molecular diameter is the length scale determining the onset of deviations from macroscopic behavior.

2.2.3.1 Phase Transitions in Confined Spaces

The theoretical foundation for describing critical phenomena in confined systems is the finite-size scaling approach [64], by which the dependence of physical quantities on system size is investigated. On the basis of the Ising Hamiltonian and finite-size scaling theory, Fisher and Nakanishi computed the critical temperature of a fluid confined between parallel plates of distance D [66]. The critical temperature refers to, e.g., a liquid/vapor phase transition. Alternatively, the demixing phase transition of an initially miscible liquid/liquid mixture could be considered. Fisher and Nakashini found that compared with free space, the critical temperature is shifted by an amount

$$\Delta T_c \propto D^{-\frac{1}{\nu}}\,. \tag{27}$$

With the critical exponent being positive, it follows that large shifts of the critical temperature are expected when the fluid is confined in a narrow space. Evans et al. computed the shift of the critical temperature for a liquid/vapor phase transition in a parallel-plates geometry [67]. They considered a maximum width of the slit of 20 times the range of the interaction potential between the fluid and the solid wall. For this case, a shift in critical temperature of 5% compared with the free-space phase transition was found. From theoretical considerations of critical phenomena

in confined geometries, not only a shift of the critical point, but also other effects as a shift in pressure with respect to the bulk fluid, are found [68]. Such theoretical results are supported by experiments on phase transitions in micro scale geometries. One of the first experimental results was obtained by Jacobs et al. [69], who studied the demixing phase transition of a binary liquid mixture in a narrow slit. They found that for a slit width of 3 μm the critical temperature is shifted by about 10 mK.

The results reported above indicate that small but measurable effects are induced when a fluid close to criticality is confined in a micro scale geometry. The reason for these effects are the long-range correlations building up in the vicinity of the critical point, i.e. the fluid starts to 'feel' the presence of the wall boundaries even at some distance away from the walls. Although, owing to their smallness, most of the effects discovered so far seem to be of limited relevance for practical applications in microfluidics, the principal mechanism of long-range correlations leaves room for significant deviations from free-space behavior on the micro scale.

2.2.3.2 Wetting and Spreading Phenomena

When the length scale of a fluidic system is reduced, surface phenomena become more and more important. On the macroscale, the physics of interfaces, moving contact lines, wetting and spreading is often masked by volumetric effects. When surface effects start to dominate, details come to light which can often be ignored in macroscopic systems but which have a measurable, sometimes decisive impact on the dynamics on the micro scale. Considerable attention has been drawn to the physics of contact lines, i.e. the boundary between immiscible fluid phases, for example liquid and vapor, and a solid surface. The static contact angle θ of the fluid interface with the solid surface is determined by Young's equation (see, e.g., [47]):

$$\cos\theta = \frac{\gamma_{SV} - \gamma_{SL}}{\gamma}, \tag{28}$$

where γ is the liquid/vapor surface tension and γ_{SV} and γ_{SL} the solid/vapor and solid/liquid free energy per unit area, respectively. Experimentally, in many situations it is observed that the contact angle is not unique, but it rather lies in some interval

$$\theta_r < \theta < \theta_a \tag{29}$$

(for an overview, see [70]). The advancing contact angle θ_a is found at the advancing front of a droplet slowly moving over a solid surface and the receding contact angle θ_r is measured at the receding front, as shown in Figure 2.6. For a droplet at rest any contact angle between θ_a and θ_r might be found, depending on the history of the dynamic evolution of the droplet, a phenomenon termed *contact angle hysteresis*.

It has been shown that contact angle hysteresis might arise as a result of inhomogeneities of the surface wetted by the liquid phase or surface roughness [70]. When surface roughness plays a considerable role, the observed contact angle may depend on the exact position of the contact line with respect to the microscopic or

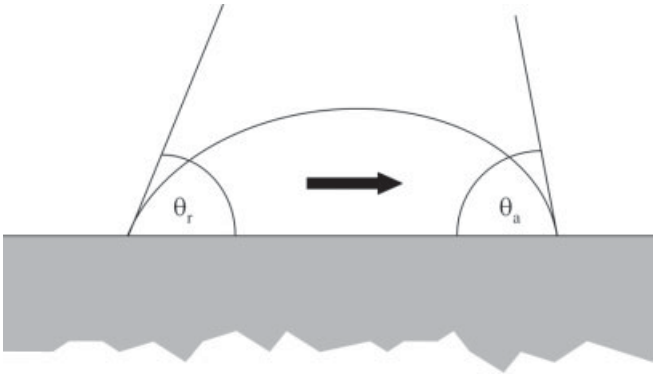

Figure 2.6 Advancing and receding contact angle for a droplet slowly moving from left to right on a solid surface.

nanoscopic structure of the surface. In a simple model with parallel grooves, different contact angles are observed depending on whether the contact line lies close to a valley or close to a crest of the surface structure [70]. Inhomogeneities might be due to chemical contamination distributed over the surface in a random fashion. Assuming a dilute distribution of such contaminations, equations for the advancing and receding contact angle have been derived [71].

While the above refers mainly to the static limit, new effects come into play when a moving contact line, i.e. spreading, is considered. It has been observed experimentally that the contact angle of a moving contact line θ_d, the dynamic contact angle, deviates from the corresponding static value θ_s. As an example, for a completely wettable surface (i.e. $\theta_s = 0$), a relationship of the form

$$u = \text{constant} \frac{\sigma \theta_d^3}{\mu} \tag{30}$$

was found (see [72] and references therein), where u is the line velocity and μ and σ are the viscosity and surface tension of the liquid. In theoretical descriptions of spreading phenomena, the motion of a wedge-like liquid profile over a solid surface is considered within the Stokes-flow regime. De Gennes [73] derived an equation which is valid for small but finite static contact angles θ_s:

$$u = \text{constant} \frac{\sigma}{\mu} \theta_d \, (\theta_s^2 - \theta_d^2) \, . \tag{31}$$

Perhaps the most complete description was given by Cox [74], who derived an expression for the dynamic contact angle which is also valid in the case of large angles. The Cox prediction was tested experimentally and a good agreement between theory and experiment was found.

Many of these results, most of them more than 10 years old, have attracted some renewed interest recently. In some μTAS and Lab-Chips small liquid volumes are transported as plugs in micro channels. Owing to the smallness of the volumes,

surface effects play a dominant role and a profound knowledge of wetting and spreading phenomena is essential for designing systems which are able to process a large number of samples in a parallel way.

2.3 Methods of Computational Fluid Dynamics

In the previous section, an overview of the physical models suitable to describe micro flow phenomena was given. Considering that the relevant length scale in micro reactors is often of the order of 100 µm, the macroscopic continuum models for momentum, heat and mass transfer can be employed in many cases. The first corrections to the macroscopic description typically appear as modifications of the flow boundary condition, such as the introduction of a finite slip length for gas flows. Hence, in many cases, the problem of simulating a micro reactor is, at least formally, equivalent to the problem of solving the corresponding continuum transport equations with suitable boundary conditions. Numerical solution strategies for the partial differential equations (PDE) describing momentum, heat and mass transfer, termed 'Computational fluid dynamics' (CFD), are the main subject of this section. Such an approach, based on a fundamental set of physical models and thorough mathematical methods allowing high-accuracy solutions to be obtained, gives the most detailed insights into flow phenomena in micro reactors and the most reliable prediction of micro-reactor performance.

CFD methods have found widespread applications in conventional chemical process technology. In addition, another class of models has frequently been used, known as lumped-element or macro models. With such types of models no detailed description of flow phenomena is attempted, but rather an integral description of certain functional units used in a chemical process. Corresponding functional units could be pipes, mixers, separators and certain types of reactors. With macro models the transformation and exchange of matter and energy in and between the functional units are described. The functional units are characterized by a number of ports by which they interact with their environment, very similar to the elements of an electronic circuit. As an example, a pipe has an inlet and an outlet port, and the volume flow inside depends on the difference in pressure between inlet and outlet. The details of the flow field inside the pipe are not taken into account explicitly, only in an integral manner via the relationship between pressure drop and volume flow. From this example it is apparent that the accuracy of macro models strongly depends on the quality of the characteristic diagrams and characteristic curves determining the relationship between the response of the system and the excitation at the ports. Typically, several functional units are combined in a conservative network, i.e. a model which guarantees that fundamental quantities such as the volumetric flow rate can distribute over the network, but are conserved as a function of time. By their descriptive nature, relying on integral relationships, macro models are well suited to complex problems allowing a large number of degrees of freedom to be subsumed into a comparatively simple characteristic diagram. An

overview of macro models used in the field of chemical process technology is given by Hlavacek et al. [75].

While the use of lumped elements is not necessarily related to a loss in accuracy, it bears two major disadvantages: reduced flexibility and an at best indirect link with the underlying physical models. The reduced flexibility becomes obvious when a number of different designs or geometries of a micro reactor have to be considered. In general, the formulation of accurate macro models is a very expensive process, making a number of validation experiments necessary. When design modifications are taken into account, it is *a priori* unclear how the corresponding macro model has to be modified. In the worst case, the whole expensive process of model formulation and validation has to be repeated. Related to that is the indirect link to physical models. When physical parameters such as density or viscosity are modified, the consequences for the macro model description are often difficult to overlook. Sometimes it is even unclear if a macro model remains valid or if new phenomena occur which would require the use of a refined model. For these reasons, macro models have not yet found extensive use in the field of micro process technology, a fact underpinned also by the application examples presented in this chapter. Instead, standard methods for the simulation of micro reactors are based on solution strategies for the partial differential equations of the underlying physical models.

The three most widespread methods for solving the transport equations for momentum, matter and heat are the finite-difference [76], the finite-element [77, 78] and the finite-volume [79] approaches. In computational fluid dynamics, typically equations of convection–diffusion type:

$$\frac{\partial(\rho\,\Phi)}{\partial t} + \frac{\partial(\rho\,u_i\,\Phi)}{\partial x_i} = \frac{\partial}{\partial x_i}\left(\Gamma\frac{\partial\Phi}{\partial x_i}\right) + S_\Phi \tag{32}$$

are to be solved. In this expression ρ and u_i are the density and the velocity of the fluid and Γ is diffusivity. The equation describes the transport of a field quantity Φ by convection (second term on the left-hand side) and diffusion (first term on the right-hand side), supplemented by a source term S_Φ. As an example, the incompressible Navier–Stokes equation could be considered. In that case Φ would be a component of the linear momentum per unit volume. The three methods indicated above are based on different strategies to obtain approximate solutions Φ. All of the methods rely on a discretization of the computational domain, i.e. a numerical grid. The different types of grids will be discussed later in Section 2.3.3. In order to classify the two most important types beforehand, a structured (left) and an unstructured (right) grid are displayed in Figure 2.7. A 2-D structured grid consists of quadrilateral elements and is, apart from a few special cases, topologically equivalent to a rectangular grid. A 2-D unstructured grid has a more general connectivity of computational cells and can be constructed from triangular or quadrilateral elements or a mixture of these.

Within the finite-difference method (FDM), the derivative terms appearing in Eq. (32) are approximated by finite-difference expressions at each grid node. As an

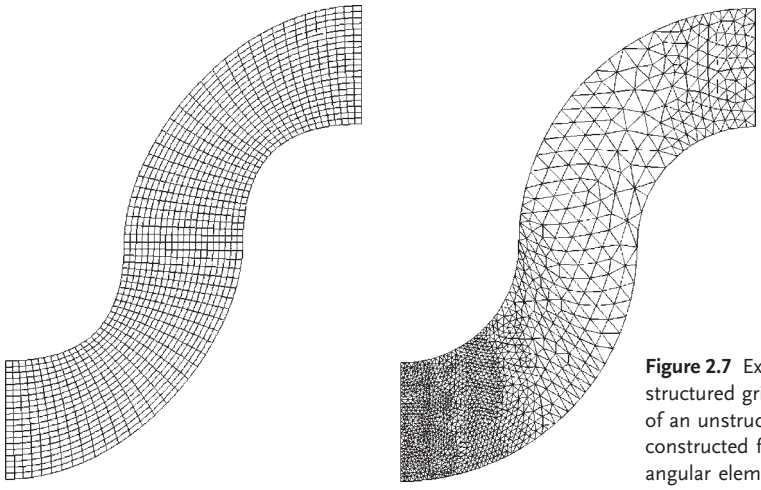

Figure 2.7 Example of a structured grid (left) and of an unstructured grid constructed from triangular elements (right).

example, on a one-dimensional grid a derivative of a function at point i could approximately be expressed via the values of this function at points $i-1$ and $i+1$ via a Taylor expansion. By these means a partial differential equation is transformed into a system of algebraic equations for the field values at the grid nodes. The advantage of the FDM is that it is very easy to implement on a rectangular or on a structured grid. However, on more complex grid geometries a FDM formulation can be challenging. A major disadvantage is the fact that the FDM is in general not a *conservative* discretization scheme. Often, the governing transport equations conserve local flow quantities such as mass or momentum. If a numerical approximation scheme does not fulfil the same conservation laws, serious deviations from the exact solution may be induced, as is often found within the FDM.

The finite-volume method (FVM) is closely linked with the FDM in so far as a partial differential equation is transformed into a system of algebraic equations for the field values at the grid nodes. However, within the FVM the system of algebraic equations is obtained by integrating the differential equation over so-called control volumes embracing the grid nodes and expressing the corresponding volume and surface integrals by the field values at the grid nodes. In this way the conservation laws are enforced and a conservative discretization scheme is obtained. The FVM has been applied also to complex grid geometries.

The finite-element method (FEM) is based on shape functions which are defined in each grid cell. The unknown function Φ is locally expanded in a basis of shape functions, which are usually polynomials. The expansion coefficients are determined by a Ritz–Galerkin variational principle [80], which means that the solution corresponds to the minimization of a functional form depending on the degrees of freedom of the system. Hence the FEM has certain optimality properties, but is not necessarily a conservative method. The FEM is ideally suited for complex grid geometries, and the approximation order can easily be increased, for example by extending the set of shape functions.

In computational fluid dynamics only the last two methods have been extensively implemented into commercial flow solvers. Especially for CFD problems the FVM has proven robust and stable, and as a conservative discretization scheme it has some built-in mechanism of error avoidance. For this reason, many of the leading commercially available CFD tools, such as CFX4/5, Fluent and Star-CD, are based on the FVM. The outline on CFD given in this book will be based on this method; however, certain parts of the discussion also apply to the other two methods.

2.3.1
Fundamentals of the Finite–volume Method

The FVM is based on a computational grid with nodes being embraced by control volumes. The values of Φ at the grid nodes are the unknowns to be solved for. An example of a 2-D computational grid with rows labeled by an index j and columns by i is displayed in Figure 2.8. It shows a grid node P embraced by a control volume (shaded in gray) and surrounded by four other nodes *N(orth)*, *S(outh)*, *W(est)*, *E(ast)*. The essential step in deriving a FV approximation is the integration of Eq. (32) over control volumes. For a stationary problem (i.e. a vanishing time derivative) the resulting equation is

$$\int_{S_{ij}} \rho\, u_i\, \Phi\, n_i\, \mathrm{d}S = \int_{S_{ij}} \Gamma \frac{\partial \Phi}{\partial x_i}\, n_i\, \mathrm{d}S + \int_{V_{ij}} S_\Phi\, \mathrm{d}V\ . \tag{33}$$

where V_{ij} denotes the volume of cell (i,j), S_{ij} its surface and n_i the components of an outward normal vector. The surface integrals are obtained from volume integrals via the Gauss theorem. The volume integral appearing on the right-hand side of the equation can easily be approximated:

$$\int_{V_{\mathrm{ij}}} S_\Phi\, \mathrm{d}V \approx (S_\Phi)_\mathrm{P}\, V_{\mathrm{ij}}\ , \tag{34}$$

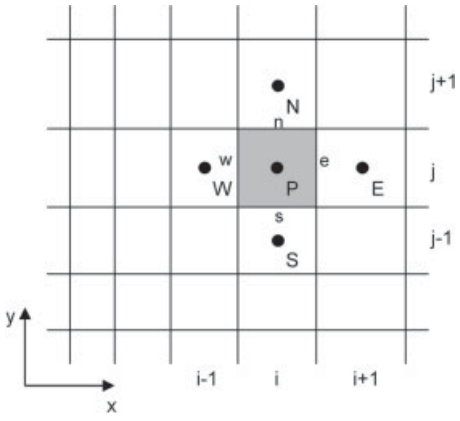

Figure 2.8 2-D FVM grid with a control volume embracing a node *P*. The grid node is surrounded by four neighboring nodes *N*, *S*, *W* and *E*.

where $(S_\Phi)_P$ denotes the value of the source term at node *P*. As only the nodal values of the unknown function should enter the FVM equations, the surface integrals have to be expressed in approximate form via Φ_P, Φ_N, Φ_S, Φ_W and Φ_E. The surface integrals can be split into four contributions from the *n*, *s*, *w*, and *e* faces. In approximate form, the contribution from the east face to the surface integral of the convective term can be written as

$$\int_{(S_{ij})_e} \rho\, u_x\, \Phi \, \mathrm{d}S \approx (\rho\, u_x\, \Phi)_e\, (S_{ij})_e \,. \tag{35}$$

A priori, neither the value of Φ nor the values of density and velocity are known at the faces of the control volume. They have to be determined via interpolation from their values at neighboring nodes. A simple approximation would be

$$\Phi_e \approx \frac{1}{2}(\Phi_P + \Phi_E) \tag{36}$$

in the case of an equidistant grid. Similar equations can be used to approximate the derivative $\partial\Phi/\partial x_i$ appearing in the diffusive term. Expressions as such Eq. (36) induce a nearest-neighbor coupling of grid nodes: the value Φ_P depends on the field values at the neighboring nodes *N*, *S*, *W* and E. In three spatial dimensions, two more nodes, *H(igh)* and *L(ow)*, are coupled to P. In total, such a nearest-neighbor coupling leads to a system of algebraic equations of the form

$$a_P\, \Phi_P = \sum_i a_i\, \Phi_i + b_P \,, \tag{37}$$

where the summation is over neighboring nodes. The coefficients a_i depend on the approximation scheme used to determine the field values on the control volume faces, while b_P depends on the form of the source terms appearing in Eq. (33). In matrix form, the system of equations can be written as

$$A\, \Phi = b \,, \tag{38}$$

where Φ represents the vector of unknowns, *A* the matrix of coefficients appearing in Eq. (37) and *b* the vector of source terms.

So far the function Φ has not yet been specified; it could represent a concentration, temperature or velocity field. In the first two cases the velocity field entering Eq. (33) would be assumed as given, it could be determined from a previous FVM simulation run. Eq. (37) then represents a set of coupled linear algebraic equations for the values of Φ at the grid nodes which can be solved by the usual iterative methods for sparse systems of linear equations. When Φ stands for a component of the velocity field itself, the situation is more complex. In that case Eq. (37) is a discretized version of the Navier–Stokes equation with coefficients a_P, a_i depending on the unknown velocity components themselves. The problem then reduces to solving a set of non-linear, coupled algebraic equations which is, however, significantly more difficult than the linear problem obtained for a temperature or concentration field.

Numerical schemes such as Eq. (36) for computing the field values at the control volume faces from the corresponding values at the surrounding nodes are of key importance within the FVM. Such so-called *differencing schemes* have a major influence on the accuracy and boundedness of the numerical solution as well as on the stability of iterative equation solvers. Especially the discretization of the convective term was found to be central to the FVM and is has been investigated in much detail in the past decades (see, e.g., [79]). In some sense the simplest differencing scheme is given by Eq. (36) and known as *central differencing*. Assuming that h is the extension of a computational cell of an equidistant grid, with Eq. (36) the convective flux at the cell faces is approximated up to corrections of order h^2. A major disadvantage of the central differencing scheme is the fact that when the flow velocity exceeds a certain value, some of the coupling coefficients a_i in Eq. (37) assume a negative value [81]. Negative coupling coefficients can induce unphysical oscillations in the solution and may be a cause of potential stability problems of iterative equation solvers. Hence the central differencing scheme is rarely used in practice. Another very simple interpolation method is the *upwind scheme* which, when applied to the east face of a control volume, results in an expression of the form

$$\Phi_e = \begin{cases} \Phi_P & \text{for} \quad u_x \geq 0 \\ \Phi_E & \text{for} \quad u_x < 0 \end{cases} \tag{39}$$

It can easily be shown that for the upwind scheme all coefficients a_i appearing in Eq. (37) are positive [81]. Thus, no unphysical oscillatory solutions are found and stability problems with iterative equation solvers are usually avoided. The disadvantage of the upwind scheme is its low approximation order. The convective fluxes at the cell faces are only approximated up to corrections of order h, which leaves room for large errors on course grids.

The *hybrid scheme* (see, e.g., [81]) represents a compromise between central and upwind differencing. It is based on the idea of using central differencing at low velocities, where the coupling coefficients are all positive. At higher velocities, where at least one of the coupling coefficients changes sign, the upwind scheme is used. The switching between central and upwind differencing is done locally, i.e. the differencing scheme for a specific control volume depends on the local flow velocity. Hence, for low-velocity flows, the central differencing scheme is used at almost all control volumes and the discretization errors are approximately of order h^2. At high velocities, the upwind scheme dominates and error terms approximately of order h are found. However, stability is maintained and unphysical oscillations are avoided.

In order to increase the accuracy of the approximation to the convective term, not only the nearest-neighbor nodes, but also more distant nodes can be included in the sum appearing in Eq. (37). An example of such a higher order differencing scheme is the QUICK scheme, which was introduced by Leonard [82]. Within the QUICK scheme, an interpolation parabola is fitted through two downstream and one upstream nodes in order to determine Φ on the control volume face. The un-

known field value is taken to be the value of the interpolation curve on the control volume face. In Figure 2.9 this is exemplified for the east face of a control volume. The value of Φ on the east face is determined from the corresponding values at nodes *W*, *P* and *E*. On an equidistant grid, Φ_e is given by

$$\Phi_e = -\frac{1}{8}\Phi_W + \frac{3}{4}\Phi_P + \frac{3}{8}\Phi_E \,. \tag{40}$$

The QUICK scheme has a truncation error of order h^3. However, similarly as in the case of the central differencing scheme, at high flow velocities some of the coupling coefficients of Eq. (37) become negative.

A few years ago, a division of the European Research Community on Flow, Turbulence and Combustion assessed the status of available CFD packages and issued a set of best practice guidelines for the use of CFD methods [83]. In these guidelines, it is recommended not to use differencing schemes with a low approximation order (such as upwind) in industrial applications. However, as low-order schemes are usually numerically more robust and less prone to convergence problems, they might be used to initialize a calculation. As convergence is approached, a higher order scheme should be used.

One should bear in mind that not only the differencing scheme, but also the structure of the computational grid determines the approximation order of a numerical model. On an equidistant grid, the central differencing scheme produces a second-order truncation error. However, if the size of neighboring control volumes is different, a truncation error of order *h* is found. The effects of grid non-uniformity can be compensated by a modification of the coupling coefficients related to the grid nodes [84], which, however, introduces a considerable additional bookkeeping effort.

Besides the convective fluxes, the diffusive fluxes on the control volume faces have to be determined. As apparent from Eq. (33), an expression for $\partial\Phi/\partial x_i$ containing the nodal values of Φ is needed. In the case of an orthogonal grid aligned with the axes of a Cartesian coordinate frame, the expression

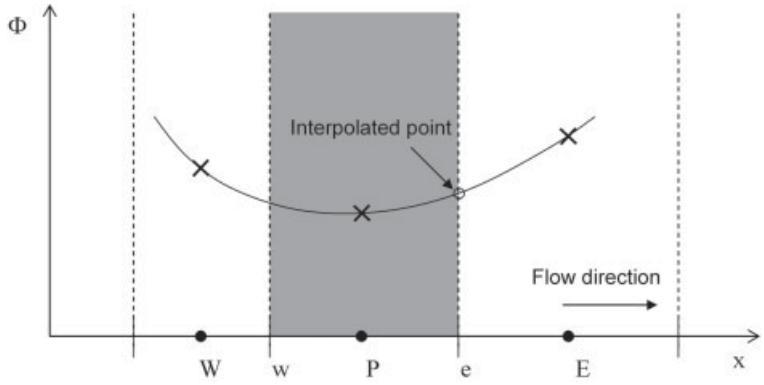

Figure 2.9 Determination of the field values on the control volume faces by interpolation within the QUICK scheme.

$$\left(\frac{\partial \Phi}{\partial x}\right)_e = \frac{\Phi_E - \Phi_P}{x_E - x_P} \tag{41}$$

for the diffusive flux in the x-direction suggests itself. Such a simple linear interpolation of the derivative terms is used as a standard within the FVM, and other differencing schemes are of minor importance.

When attempting to solve a partial differential equation such as Eq. (32) with a numerical approximation scheme, the accuracy of the approximation is a key issue for many practical applications. In chemical engineering technology, an increase in yield of a certain reaction of only 1% may be associated with a significant cost reduction. Even if in some cases numerical models with an order-of-magnitude accuracy may be useful (for example in cases where elaborate models and experimental data are not available), deviations of a few percent at the maximum between model predictions and the real world are usually demanded. Specifically in micro process technology and in microfluidics in general, there is one predominant discretization artefact often limiting the accuracy of numerical predictions: *numerical diffusion*.

The term numerical diffusion describes the effect of artificial diffusive fluxes which are induced by discretization errors. This effect becomes visible when the transport of quantities with small diffusivities [with the exact meaning of 'small' yet to be specified in Eq. (42)] is considered. In macroscopic systems such small diffusivities are rarely found, at least when being looked at from a phenomenological point of view. The reason for the reduced importance of numerical diffusion in many macroscopic systems lies in the turbulent nature of most macro flows. The turbulent velocity fluctuations induce an effective diffusivity of comparatively large magnitude which includes transport effects due to turbulent eddies [1]. The effective diffusivity often dominates the numerical diffusivity. In contrast, micro flows are often laminar, and especially for liquid flows numerical diffusion can become the major effect limiting the accuracy of the model predictions.

In order to be more explicit, the upwind differencing scheme will be considered. Again, an orthogonal computational grid aligned with the axes of a Cartesian coordinate system is assumed. When inserting the expression from the upwind scheme into the transport equation Eq. (33) and re-expressing the field values at the grid nodes by the corresponding values at the control-volume faces via a Taylor expansion, error terms of the same structure and the same sign as the original diffusive terms are found [81]. Hence the discretization error has the effect of artificially increasing the diffusive fluxes. The effective diffusion constant in the x-direction is given as

$$\Gamma_{\mathrm{eff},x} = \Gamma + \frac{u_x\, h}{2}. \tag{42}$$

The second term on the right-hand side is the numerical diffusivity, depending on the flow velocity in the x-direction, u_x, and the length of the control volume in the x-direction, h. Similar expressions hold for the other coordinate directions. Apparently, the numerical diffusion increases with increasing flow velocity and

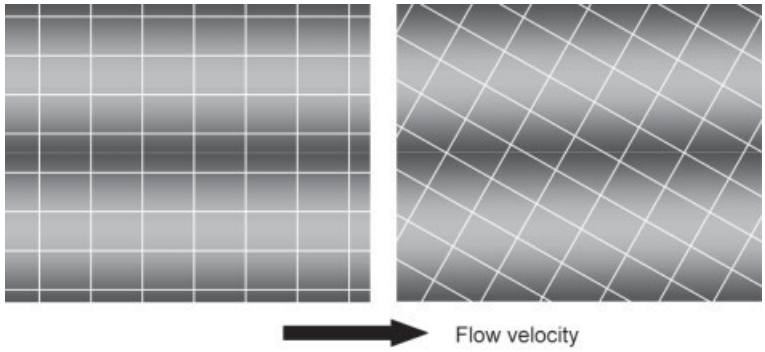

Figure 2.10 Multilamination flow oriented along the computational grid (left) and forming a tilted angle with the grid cells (right).

increasing size of the grid cells. Furthermore, it is direction dependent and depends on the relative orientation of the local flow velocity vector and the control volume.

A problem often encountered in microfluidic systems is multilaminated flow with the flow direction equal to the orientation of the fluid lamellae. An example could be a multilamination micro mixer in which thin layers with varying concentration of a solvent are created. Again assuming a computational grid aligned with the axes of a Cartesian coordinate frame, Eq. (42) shows that the numerical diffusivity perpendicular to the fluid lamellae vanishes when the flow direction coincides with the orientation of the grid. On the other hand, when the flow is not aligned with the grid, an artificial diffusive flux between different fluid lamellae is induced. This situation is depicted in Figure 2.10 where the fluid lamellae are shaded with different gray tones. On the left-hand side, the flow is aligned with the grid and numerical diffusion between different lamellae is suppressed. On the right-hand side, the velocity vector stands at some finite angle with respect to the grid cell orientation. In such a case an artificial diffusive flux between different lamellae is induced.

In practice, situations where the computational grid can be fully aligned with the local flow velocity vectors are very rare. In order to reduce discretization artefacts, a differencing scheme of higher order can be chosen. In a strict sense, higher order differencing schemes are free of numerical diffusion, as, unlike for the upwind scheme, the error terms are no longer of the same structure as the diffusive transport terms. However, discretization errors of higher order are encountered having more subtle effects than purely enhancing the diffusivity. A comparison of typical results obtained with the upwind and the QUICK scheme for a hypothetical layered flow of a solute with zero diffusivity is shown in Figure 2.11. Owing to the vanishing diffusivity, in the exact solution of the transport equations the concentration profile should be given by a step function throughout the whole flow domain. This is indicated by a dashed line. In case of misalignment of the flow with the computational grid, the upwind scheme results in a broadening of the concen-

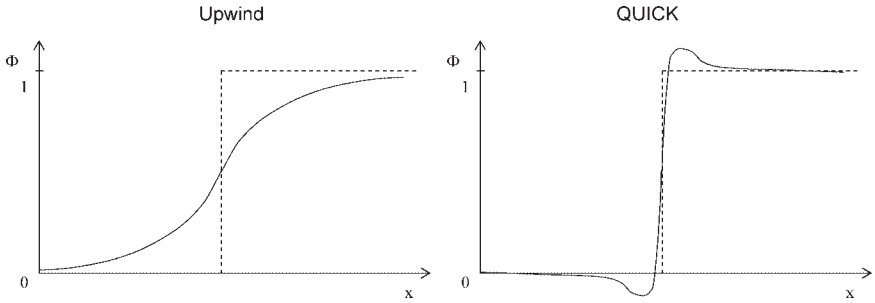

Figure 2.11 Step-function concentration profile and typical numerical results obtained with the upwind (left) and the QUICK scheme (right).

tration profile, as shown on the left. A significantly reduced broadening is found with the QUICK scheme (right). However, overshooting of the physical limits of the scalar field, which are assumed $\Phi = 1$ and $\Phi = 0$ for illustration, may occur. Even with higher order differencing schemes the modeling of convection–diffusion processes of solutes in liquid micro flows remains a challenge, and often satisfactory results are obtained only on very fine grids.

When transient problems are considered, the time derivative appearing in Eq. (32) also has to be approximated numerically. Thus, besides a spatial discretization, which has been discussed in the previous paragraphs, transient problems require a temporal discretization. Similar to the discretization of the convective terms, the temporal discretization has a major influence on the accuracy of the numerical results and numerical stability. When Eq. (32) is integrated over the control volumes and source terms are neglected, an equation of the following form results:

$$\frac{\partial \Phi}{\partial t} = A' \Phi \,, \tag{43}$$

with Φ being the vector of unknowns at the grid nodes and A' a coefficient matrix which is slightly modified compared to Eq. (38). For the sake of simplicity, a constant density was assumed and the source terms were set to zero. Often the time derivative is approximated as

$$\frac{\partial \Phi}{\partial t} \approx \frac{\Phi^{n+1} - \Phi^n}{\Delta t} \,, \tag{44}$$

where the superscripts denote the time steps n and $n + 1$. There are two major classes of time discretization schemes, *explicit* and *implicit* schemes. The explicit Euler scheme for the solution of Eq. (43) is given as

$$\frac{\Phi^{n+1} - \Phi^n}{\Delta t} = A' \Phi^n \,. \tag{45}$$

In the implicit Euler scheme, the unknown function at the new time step appears on the right-hand side.

$$\frac{\Phi^{n+1} - \Phi^n}{\Delta t} = A' \Phi^{n+1} . \tag{46}$$

Within explicit schemes the computational effort to obtain the solution at the new time step is very small: the main effort lies in a multiplication of the old solution vector with the coefficient matrix. In contrast, implicit schemes require the solution of an algebraic system of equations to obtain the new solution vector. However, the major disadvantage of explicit schemes is their instability [84]. The term stability is defined via the behavior of the numerical solution for $t \to \infty$. A numerical method is regarded as stable if the approximate solution remains bounded for $t \to \infty$, given that the exact solution is also bounded. Explicit time-step schemes tend to become unstable when the time step size exceeds a certain value (an example of a stability limit for PDE solvers is the von-Neumann criterion [85]). In contrast, implicit methods are usually stable.

For practical purposes, implicit schemes are the methods of choice when the solution is smooth and well behaved as a function of time. In that case much larger time steps can be taken than with explicit schemes, thus allowing a reduction in the computational effort. When large temporal gradients and rapid variations are expected, accuracy constraints set severe limits to the time-step size. In that case explicit schemes might be favorable, as they come with a reduced numerical effort per time step.

A method which represents a compromise between the explicit and implicit Euler scheme is the Crank–Nicolson method:

$$\frac{\Phi^{n+1} - \Phi^n}{\Delta t} = \frac{1}{2} A' \Phi^n + \frac{1}{2} A' \Phi^{n+1} . \tag{47}$$

The Crank–Nicolson method is popular as a time-step scheme for CFD problems, as it is stable and computationally less expensive than the implicit Euler scheme.

2.3.2 Solution of the Navier–Stokes Equation

The strategies discussed in the previous chapter are generally applicable to convection–diffusion equations such as Eq. (32). If the function Φ is a component of the velocity field, the incompressible Navier–Stokes equation, a non-linear partial differential equation, is obtained. This stands in contrast to Φ representing a temperature or concentration field. In these cases the velocity field is assumed as given, and only a linear partial differential equation has to be solved. The non-linear nature of the Navier–Stokes equation introduces some additional problems, for which special solution strategies exist. Corresponding numerical techniques are the subject of this section.

The flow phenomena described by the Navier–Stokes equation fall into two classes discriminated by the nature of the compressibility effects to be taken into account. For compressible flow, the Navier–Stokes equation [Eq. (1)] has to be solved in com-

bination with the mass conservation equation [Eq. (2)]. In such a case an equation of motion for the pressure field results from the mass conservation equation when an equation of state:

$$\rho = \rho(p,T) \tag{48}$$

defining a relationship between density, pressure and temperature, is utilized. As an example, Eq. (48) could represent the ideal gas law.

The situation is different for incompressible flow. In that case, no equation of motion for the pressure field exists and via the mass conservation equation Eq. (17) a dynamic constraint on the velocity field is defined. The pressure field entering the incompressible Navier–Stokes equation can be regarded as a parameter field to be adjusted such that the divergence of the velocity field vanishes.

As will be outlined below, the computation of compressible flow is significantly more challenging than the corresponding problem for incompressible flow. In order to reduce the computational effort, within a CFD model a fluid medium should be treated as incompressible whenever possible. A 'rule of thumb' often found in the literature and used as a criterion for the incompressibility assumption to be valid is based on the Mach number of the flow. The Mach number is defined as the ratio of the local flow velocity and the speed of sound. The rule states that if the Mach number is below 0.3 in the whole flow domain, the flow may be treated as incompressible [84]. In practice, this rule has to be supplemented by a few additional criteria [3]. Especially for micro flows it is important to consider also the total pressure drop as a criterion for incompressibility. In a long micro channel the Mach number may be well below 0.3, but owing to the small hydraulic diameter of the channel a large pressure drop may be obtained. A pressure drop of a few atmospheres for a gas flow clearly indicates that compressibility effects should be taken into account.

For the important case of incompressible flow, a variety of numerical schemes for computing the velocity and pressure fields have been developed. A thorough discussion of even the few most important methods would be beyond the scope of this book. The discussion will be limited to so-called pressure-correction schemes which have found widespread applications in commercial FVM solvers. The essence of the methods lies in the coupling between velocity and pressure. On computational grids with coinciding nodes for the velocity and the pressure field, unphysical oscillations of the pressure field have been observed [81]. Such small-wavelength oscillations can be avoided when a staggered arrangement of grids for velocity and pressure is chosen [86]. A simple one-dimensional example of a staggered grid is displayed in Figure 2.12, together with the standard arrangement with colocated variables. In the colocated arrangement the nodes at which the velocity and the pressure variables are defined coincide. In the case of staggered grids, the pressure nodes are located on the control volume faces of the velocity grid. As staggered grids require an additional bookkeeping effort, especially for complex geometries, interpolation schemes for the velocity field have been developed which allow one to suppress the unphysical pressure oscillations [87]. These methods have to some degree rendered the staggered arrangement superfluous and have found widespread applications in commercial FVM solvers.

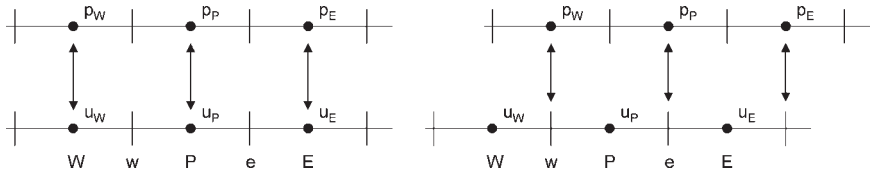

Figure 2.12 Computational grids with colocated (left) and staggered (right) arrangement of the velocity and pressure nodes.

A discretized version of the steady-state incompressible Navier–Stokes equation derived from Eq. (16) can be written as

$$a_P^{u_i}\ u_{i,P} + \sum_l a_l^{u_i}\ u_{i,l} = b_{i,P} - \left(\frac{\partial p}{\partial x_i}\right)_P . \tag{49}$$

In this expression, a node P is coupled to neighboring nodes l via coupling coefficients $a_l^{u_i}$ which themselves depend on the unknown velocity values u_i. The source term $b_{i,P}$ represents gravity or other volumetric forces. The spatial derivative of pressure taken at node P stands for any discrete version of this expression, either evaluated on a colocated or a staggered grid. The goal is to solve Eq. (49) in combination with the mass conservation equation Eq. (17). The basic idea of a pressure correction scheme is to begin an iterative procedure with a guess for the pressure field, denoted as p^{m-1}, and a corresponding guess for the velocity field u_i^{m-1}. Subsequently, a first approximation $u_i^{(1)\,m-1}$ for the new velocity field is computed by solving the equation

$$a_P^{u_i^{m-1}}\ u_{i,P}^{(1)m} + \sum_l a_l^{u_i^{m-1}}\ u_{i,l}^{(1)m} = b_{i,P} - \left(\frac{\partial p^{m-1}}{\partial x_i}\right)_P . \tag{50}$$

At that stage, the approximation obtained for the velocity field does generally not fulfil the mass conservation equation. In order to ensure mass conservation, corrections to the velocity and pressure field are introduced via

$$u_i^m = u_i^{(1)m} + u_i', \quad p^m = p^{m-1} + p' . \tag{51}$$

By demanding that the new velocity u_i^m field fulfils both the momentum and the mass conservation equation, the following equations for the velocity and pressure correction are derived:

$$a_P^{u_i^{m-1}}\ u_{i,P}' + \sum_l a_l^{u_i^{m-1}}\ u_{i,l}' = -\left(\frac{\partial p'}{\partial x_i}\right)_P , \tag{52}$$

$$\frac{\partial}{\partial x_i}\left[\frac{1}{a_P^{u_i^{m-1}}}\left(\frac{\partial p'}{\partial x_i}\right)\right]_P = \left(\frac{\partial u_i^{(1)m}}{\partial x_i}\right)_P - \frac{\partial}{\partial x_i}\left(\frac{1}{a_P^{u_i^{m-1}}}\sum_l a_l^{u_i^{m-1}}\ u_{i,l}'\right)_P . \tag{53}$$

By solving the pressure and velocity correction equations, the corresponding correction terms and thus the new velocity field u_i^m, which by construction fulfils the mass conservation equation, can be determined. However, in general a single correction step does not yield a solution of the Navier–Stokes equation, the reason for this fact being traced back to Eq. (52) and Eq. (50). The coupling coefficients $a_P^{u_i^{m-1}}$ appearing in these equations are evaluated with the help of the old velocity values u_i^{m-1}. Hence u_i^m does not represent a self-consistent solution of the Navier–Stokes equation and further iterations are required to obtain the final solution. For this purpose p^m and u_i^m are chosen as new initializations and the procedure described above is repeated until convergence is achieved.

In practice, the full versions of the pressure and velocity correction equation are rarely considered. In order to determine the velocity correction, the sum over neighboring nodes:

$$\sum_l a_l^{u_i^{m-1}} u'_{i,l} \tag{54}$$

appearing in Eqs. (52) and (53) would require a linear system of equations to be solved at each iteration. As this would introduce a considerable numerical effort, some simplifications are usually made. The most drastic approximation is to disregard completely the sum over neighboring nodes. Such a modification leaves the final values of the pressure and the velocity field unaffected, as for a fully converged solution the corrections are zero and the neglect of a vanishing term does not alter the determining equations. The corresponding method is known as the SIMPLE algorithm [88]. The SIMPLE algorithm is prone to convergence problems and usually requires under relaxation. For this reason, a slightly more complicated but yet more robust method has been devised. Instead of neglecting the sum over neighboring nodes it is approximated as

$$\sum_l a_l^{u_i^{m-1}} u'_{i,l} \approx u'_{i,P} \sum_l a_l^{u_i^{m-1}} . \tag{55}$$

A pressure correction scheme based on such an approximation is known as the SIMPLEC algorithm [89]. The SIMPLEC algorithm does not require under relaxation of the pressure correction, is efficient and has found widespread applications.

Compared with incompressible flow, the computation of compressible flow is significantly more involved. In a compressible medium, sound waves may propagate and may induce complicated spatio-temporal patterns superposed on the flow. For transsonic and supersonic flows, non-linear wave phenomena, so-called shock waves, are observed. Shock waves are sharp wave fronts where flow quantities such as density or pressure change in a discontinuous manner. In order to capture shock fronts numerically, very fine grids in the close vicinity of the shock are needed. As the location of the shock fronts is *a priori* unknown, meshes with adaptive grid refinement are required to describe corresponding flow phenomena with a reasonable degree of accuracy while keeping the numerical effort within tolerable limits [90, 91]. Even without shock waves compressible flows bear some additional nu-

merical challenges. For incompressible flow the scale of the numerical time-step size is governed by the time it takes the fluid to convect through a single computational cell. When compressible flow is considered, a new time-scale is introduced via the speed of sound and the corresponding time a sound wave takes to propagate through a computational cell. If the speed of sound is much larger than the flow velocity, the allowable time-step size in a numerical computation of compressible flow phenomena might be much smaller than the corresponding quantity for incompressible flow.

Another principle difference of compressible flow computations as compared with incompressible flow is an enhanced coupling of the governing equations. Via the equation of state Eq. (48) a change in density is in general related to a temperature change. Vice versa, via convective transport of heat the velocity field has a substantial impact on the spatio-temporal temperature distribution. On the other hand, a change in temperature may induce a flow via the induced change in density. Hence there is a two-way coupling between the Navier–Stokes equation and the enthalpy equation. Another effect adding to the coupling is viscous heating. The viscosity term in the Navier–Stokes equation:

$$\frac{\partial}{\partial x_k}\left[\mu\left(\frac{\partial u_i}{\partial x_k}+\frac{\partial u_k}{\partial x_i}-\frac{2}{3}\,\delta_{ik}\,\frac{\partial u_j}{\partial x_j}\right)\right] \tag{56}$$

describes the dissipation of kinetic energy into heat. Consequently, from this term a source term for the enthalpy equation can be derived (see, e.g., [29]). The coupling of the momentum and the enthalpy equation induced is not only restricted to compressible flow, but in principle has to be considered in the case of incompressible flow also. However, the corresponding effect, known as viscous heating, is of only minor importance in many practical cases. A phenomenon of notable importance in practice is the temperature dependence of the dynamic viscosity. For non-isothermal, compressible and incompressible flow it should be taken into account that the viscosity depends on temperature and that the corresponding relationship allows the temperature field to have an effect on the flow field.

For the computation of compressible flow, the pressure–velocity coupling schemes previously described can be extended to pressure–velocity–density coupling schemes. Again, a solution of the linearized, compressible momentum equation obtained with the pressure and density values taken from a previous solver iteration in general does not satisfy the mass balance equation. In order to balance the mass fluxes into each volume element, a pressure, density and velocity correction on top of the 'old' values is computed. Typically, the detailed algorithms for performing this task rely on the same approximations such as the SIMPLE or SIMPLEC schemes outlined in the previous paragraph.

2.3.3 Computational Grids

The quality of the numerical grid is essential for the accuracy of the numerical results obtained in a CFD calculation. Not only the size but also the geometric shape of the grid cells determines the discretization errors of the numerical approximation. Whereas 20 years ago only simple geometries with a comparatively small number of degrees of freedom could be considered, nowadays even standard workstations allow the study of flow phenomena in complex geometries on grids with several million cells. This necessitates highly automated methods for the generation of high-quality grids.

Given a geometric model of the flow domain to be considered, the problem is to create a grid which is ideally adjusted to the geometry and produces comparatively small numerical errors. The latter requirement can be translated to an adjusted spatial variation of the grid resolution. Ideally, the grid should be fine in regions where large gradients of the computed field quantities are found, whereas it can be comparatively coarse in the rest of the computational domain. The decision on where to provide a high-mesh density is often left to the user. An experienced user is usually able to predict some of the regions where high numerical accuracy is needed, but even an expert will experience occasional surprises. In contrast, in the past few years some powerful automated methods for local grid refinement on the basis of *a posteriori* error estimates and target functions have been developed [92, 93]. However, the discussion of such methods is beyond the scope of this book, which can only scratch the surface of the most common techniques of computational fluid dynamics. In the following paragraphs an overview of the different types of grids, including a brief discussion of their advantages and disadvantages, is given.

There are at least two different ways to adjust a computational grid to the geometry of the flow domain. One strategy is to overlay a Cartesian grid on the domain and to approximate those parts of the domain boundary which are not parallel to the coordinate directions by a stepwise borderline. Sample geometry with a corresponding Cartesian grid is shown on the left side of Figure 2.13. Another strategy is to give up the requirement for orthogonality and to adjust the grid geometry in such a way that the domain boundary coincides with the boundary of the grid. Such a body-fitted grid is shown on the right side of Figure 2.13.

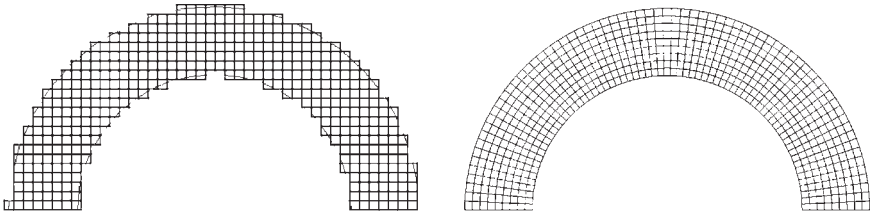

Figure 2.13 2-D Cartesian (left) and body-fitted grid (right) defined on a curved pipe.

The advantage of a Cartesian grid is the fact that discretization schemes can be easily implemented on a rectangular geometry. However, the approximation of the domain boundary by a step function is often poor and, correspondingly, boundary conditions are implemented only in a very crude fashion. In contrast, body-fitted grids allow for an unproblematic implementation of boundary conditions. Furthermore, with body-fitted grids, numerically optimal configurations such as grid cells aligned with the flow direction are often easier to achieve. As an example, the grid cells of the body fitted grid in Figure 2.13 are to a large degree aligned with the flow. According to the discussion in Section 2.3.1, an alignment of the velocity vectors with the grid cells guarantees a minimum degree of numerical diffusion. The disadvantage of body-fitted grids lies in the numerical complexity and a somehow increased computational effort related to solving the transport equations on a non-orthogonal grid. Nevertheless, body-fitted grids have found widespread applications in commercial CFD solvers, for which they have become almost a standard.

The standard way of implementing the transport equations for momentum, heat and matter on a body-fitted grid is based on mapping the complex flow domain in physical space to a simple (for example rectangular) flow domain in computational space. This is achieved via a curvilinear coordinate transformation. As an example, for the problem of computing the flow field in a curved pipe the physical domain shown on the left hand side of Figure 2.14 is mapped to a simple rectangular domain in computational space. The simple grid geometry in computational space has the advantage that discretization of the transport equations is comparatively straightforward. However, through the curvilinear coordinate transformation a number of extra terms in the transport equations are introduced, examples of which are the centrifugal or the Coriolis force in the transformed momentum equation.

For the example in Figure 2.14 it would be possible to perform the coordinate transformation analytically by introducing cylindrical coordinates. However, in general, geometries are too complex to be described by a simple analytical transformation. There are a variety of methods related to numerical curvilinear coordinate transformations relying on ideas of tensor calculus and differential geometry [94]. The fundamental idea is to establish a numerical relationship between the physical space coordinates x_i and the computational space curvilinear coordinates ξ_i. The local basis vectors of the curvilinear system are then given as

$$(\mathbf{e})_i = \frac{\partial \mathbf{x}}{\partial \xi_i} \tag{57}$$

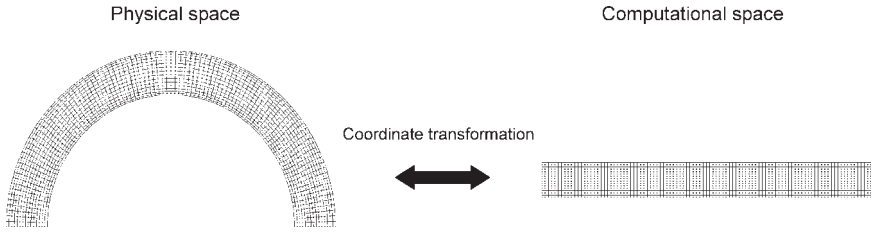

Figure 2.14 Example of a grid structure in physical space (left) and in computational space (right).

and the transport equation for a field quantity Φ can be transformed by means of the relationship

$$\frac{\partial \Phi}{\partial \xi_i} = \frac{\partial \Phi}{\partial x_j} \frac{\partial x_j}{\partial \xi_i} . \tag{58}$$

When facing the task of creating a computational grid for solving a fluid flow problem, a decision has to be made whether a structured or an unstructured grid is more suited for the problem under consideration. An example of 2-D structured and unstructured grids was given in Figure 2.7. A *structured grid* typically consists of quadrilateral or hexahedral cells and is defined according to the specifications of the user. In order to define a structured grid, the flow domain is divided into several blocks which are topologically equivalent to quadrilaterals (in 2-D) or hexahedra (in 3-D). Subsequently, the user has to specify subdivisions on the edges of the blocks which are directly used to define a grid of quadrilateral or hexahedral cells within the blocks. Inside each block a grid cell can be uniquely identified by a set of indices. For example, in two dimensions a label (*i,j*) denotes a cell in the *i*th column and *j*th row, where rows and columns are aligned with the local coordinate system of the block. The advantage of a structured grid is the fact that owing to the regular geometry of the computational cells, discretization errors related to specific differencing schemes for the various terms in the transport equations are minimized. A disadvantage of structured grids is related to local adaptation to steep gradients or sudden changes of the field quantity to be determined. Owing to the simple construction scheme of structured grids, it is very difficult to enhance the grid density in localized regions. Typically, in order to refine the grid at a specific point in space, the grid density has to be enhanced also in other regions where owing to the lack of steep gradients a lower grid density would be sufficient. As a further disadvantage, in complex geometries it can be very difficult or time consuming to define a structured grid. The standard approach to overcome such problems is the automatic generation of an unstructured grid.

In many fields of engineering, *unstructured grids* represent the only way to study flow phenomena in realistic geometries. Nowadays, CDF simulations based on unstructured grids of the scale of multi-million grid cells can be run even on standard workstations. In Figure 2.15 an example of a fluidic connector meshed with an unstructured grid is displayed. Typically, an unstructured grid consists of triangular (in 2-D) or tetrahedral (in 3-D) cells. The cell connectivity of such a grid is more complex than for an unstructured grid and a simple labeling of the cells with row and column indices is no longer possible. An advantage of unstructured grids is the fact that they can be created in a highly automated way, with minimum user input required. A further important aspect of automated grid generation is the possibility of automatic grid refinement according to local properties of the solution field. The only efficient way to adjust the grid density locally in response to a current approximation to the computed field quantities is an automatic subdivision of the grid cells. Even when no automatic refinement based on a sequence of grids is necessary and a single grid is sufficient, unstructured grids offer ways to

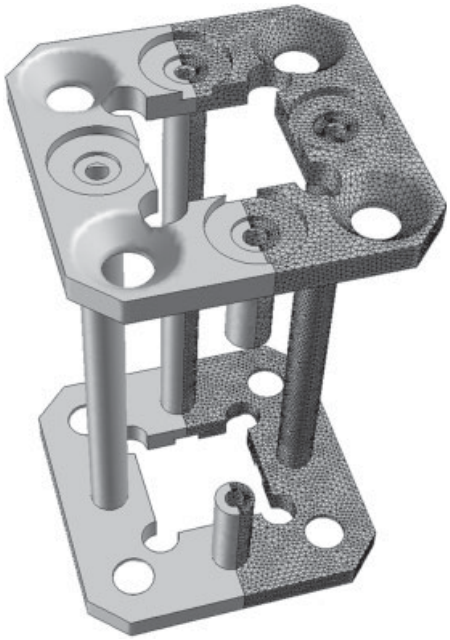

Figure 2.15 Fluidic connector with an unstructured tetrahedral grid.

adjust the grid density in localized regions in space unparalleled by structured grids. The disadvantage of unstructured grids is a reduced accuracy due to the lower approximation order of many differencing and interpolation schemes when implemented on triangular or tetrahedral geometries.

Algorithms for the generation of unstructured meshes usually start on the boundary of the domain, for example in the three-dimensional case first a surface grid is created. After that, tetrahedra with a base on the surface are formed and the algorithm subsequently works its way towards the center of the domain. Frequently used algorithms for unstructured mesh generation are the advancing front method [95] and the method of Delaunay triangulation [96].

In addition to the grid density, the quality of a grid depends on a number of other factors such as the aspect ratio of the cells and the relative size of neighboring cells. A comprehensive listing of the quality criteria for computational grids is given elsewhere [83]. Some of the important points to be remembered are:

- Highly skewed cells should be avoided. The angles between the grid lines of a hexahedral mesh should be ~ 90°. Angles < 40° or > 140° often imply a reduced accuracy or numerical instabilities.
- The aspect ratio of hexahedral cells should be not too high, typically below 20–100. If high-aspect ratio cells are used, the accuracy and possible convergence problems depend greatly on the flow direction.
- The mesh expansion ratio, i.e. the size ratio of neighboring cells, should be kept small. Particularly in regions of large gradients, mesh size discontinuities should be avoided.

2.3.4 Solution Methods for Linear Algebraic Systems

The efficiency of modern CFD solvers relies heavily on the availability of fast solution methods for linear systems of algebraic equations. In the course of a CFD simulation, linear equation systems such as Eq. (38) have to be solved successively. The problem to be solved might be a linear one in itself, as would be the case for heat transfer phenomena. Then, given a steady-state problem, a single solution of Eq. (38) suffices to determine the unknown field quantity Φ in the whole computational domain. In the case of time-dependent linear problems, a linear algebraic system usually has to be solved for each time step. Finally, an inherently non-linear problem such as the solution of the Navier–Stokes equation requires successive solution of a system such as Eq. (38) in the course of the iteration process set up to solve the resulting non-linear algebraic system. If, in that context, a time-dependent problem is considered, a nested set of computational tasks consisting of successive time steps, successive non-linear iterations and successive solutions of linear algebraic systems is obtained. Thus, fast solution methods for linear equation systems are of paramount importance for any CFD solver.

In principle, the task of solving a linear algebraic systems seems trivial, as with Gauss elimination a solution method exists which allows one to solve a problem of dimension N (i.e. N equations with N unknowns) at a cost of $O(N^3)$ elementary operations [85]. Such solution methods which, apart from roundoff errors and machine accuracy, produce an exact solution of an equation system after a predetermined number of operations, are called *direct solvers*. However, for problems related to the solution of partial differential equations, direct solvers are usually very inefficient. Methods such as Gauss elimination do not exploit a special feature of the coefficient matrices of the corresponding linear systems, namely that most of the entries are zero. Such sparse matrices are characteristic of problems originating from the discretization of partial or ordinary differential equations. As an example, consider the discretization of the one-dimensional Poisson equation

$$\frac{\mathrm{d}^2\Phi}{\mathrm{d}x^2} = f(x) \tag{59}$$

by means of a simple finite-difference approach on a uniform grid. The resulting system of linear algebraic equations is given as

$$\frac{1}{(\Delta x)^2}(\Phi_{i-1} - 2\,\Phi_i + \Phi_{i+1}) = f_i\,, \tag{60}$$

where Δx is the grid spacing. From Eq. (60), it is obvious that a node i is coupled only to the neighboring nodes $i - 1$ and $i + 1$. The corresponding coefficient matrix has entries only along its diagonal and along two bands above and below the diagonal.

In order to exploit the sparseness of the matrix, *iterative solvers* can be applied. The iterative procedure is initialized with a guess for the solution vector Φ. In

subsequent iterations this guess is successively improved until the required accuracy is reached. In general, iterative solvers produce an exact solution of a linear algebraic system only after an infinite number of iterations. However, as even direct solvers never produce exact results owing to roundoff errors, iterative solvers might yield approximations of comparable accuracy after a comparatively small number of iterations. In addition, there are inaccuracies related to the spatial and temporal discretization, and it is in general not useful to require a higher accuracy from the equation solvers than inherent in the discretization scheme. For large linear systems, iterative solvers are usually much more efficient than direct solvers. In general, an analytical expression for the operation count of iterative solvers as a function of the problem dimension cannot be derived. However, for the case of the numerical solution of the Poisson equation sketched above, the operation count of iterative solvers required for obtaining an approximate solution with relative accuracy ε can be computed analytically. Compared with Gauss elimination with its $O(N^3)$ effort, iterative solvers show a much better performance. Examples are the conjugate gradient method with its $O(N^{3/2} \ln\varepsilon)$ and the full multigrid method with its $O(N)$ operation count [97].

The general structure of an iterative solution method for the linear system of Eq. (38) is given as

$$M \, \Phi_{n+1} = N \, \Phi_n + b \, , \tag{61}$$

with

$$A = M - N \, . \tag{62}$$

The iteration scheme allows to compute an improved approximation Φ_{n+1} given a previous approximation Φ_n as an input. If after a number of iterations $\Phi_{n+1} \approx \Phi_n$ (i.e. the iteration scheme has converged), an approximate solution to the linear algebraic system has been found. The choice of the matrices M and N determines the specific form of the iterative solution scheme. After n iterations, the approximate solution will in general not satisfy the linear equation system exactly, but a non-zero residual ρ_n will remain, defined via

$$A \, \Phi_n = b - \rho_n \, . \tag{63}$$

In CFD, a number of different iterative solvers for linear algebraic systems have been applied. Two of the most successful and most widely used methods are *conjugate gradient* and *multigrid methods*. The basic idea of the conjugate gradient method is to transform the linear equation system Eq. (38) into a minimization problem

$$F = \Phi^{\mathrm{T}} \, A \, \Phi - \Phi^{\mathrm{T}} \, b \overset{!}{=} \min. \tag{64}$$

If the matrix A is positive definite, i.e. it is symmetric and has positive eigenvalues, the solution of the linear equation system is equivalent to the minimization of the bilinear form given in Eq. (64). One of the best established methods for the solution of minimization problems is the method of steepest descent. The term 'steepest descent' alludes to a picture where the cost function F is visualized as a land-

scape of hills and valleys in an N-dimensional space. In order to find a minimum of F starting from a specific point in that N-dimensional space, one simply walks 'downhill', i.e. in the direction of the negative gradient of F. A simple strategy would be to minimize F along a line defined by the negative gradient, compute the gradient at the minimum point determined in such a way, do another line minimization, etc. Often, in practice this strategy is not very efficient, as the search direction may oscillate rapidly without substantially lowering the value of the cost function. It is in fact not advisable always to take the steepest descent, rather the search should be performed along directions which are *conjugate* to each other. Two unit vectors e_1 and e_2 are conjugate with respect to a matrix A if they satisfy

$$e_1^{\mathrm{T}} \, A \, e_2 = 0 \, . \tag{65}$$

If a line minimization along e_1 is followed by a minimization along a conjugate direction e_2, the second minimization will avoid undoing what has been achieved in the first minimization as far as possible. In fact, it can be proven that the minimum of the cost function can be found by means of N subsequent line minimizations along conjugate directions [98]. However, the number of iterations required to find the exact solution will be very large for a typical CFD problem. For this reason, it is advisable to view the conjugate gradient method not as an algorithm to find exact solutions to systems of linear equations, but rather as an iterative scheme to determine approximate solutions. One of the essential ingredients of the conjugate gradient method is an algorithm for finding conjugate unit vectors with respect to the coefficient matrix under study. There exist methods which allow one to determine a unit vector conjugate to an already existing set of unit vectors [98]. In this way it is possible to start with one search direction and to subsequently generate new search directions which are optimal in the sense described above.

In practice, it is necessary to supplement and modify the basic principles described here. The coefficient matrix A will in general not be positive definite, so first the problem has to be transformed into one to which a minimization procedure is applicable [170]. In addition, without further provisions, convergence of the conjugate gradient method will be slow. The convergence speed of the method depends on the condition number of the matrix A, which is the ratio of the largest and the smallest eigenvalue. It is advisable first to do a transformation which improves the condition number before the conjugate gradient method is started. Hence the conjugate gradient method is applied to a transformed linear system of the form

$$\tilde{A}^{-1} \, A \, \Phi = \tilde{A}^{-1} \, b \, . \tag{66}$$

The matrix $\tilde{A}$ is known as the preconditioner and has to be chosen such that the condition number of the transformed linear system is smaller than that of the original system.

In contrast to the conjugate gradient method, the multigrid method is rather a general framework for iterative solvers than a specific method. The multigrid method exploits the fact that the iteration error

$$\varepsilon_n = \Phi - \Phi_n \tag{67}$$

often behaves in a very well-defined way as a function of the iteration number n. The iteration error is, similarly to Φ, a field quantity and depends on the spatial coordinates. It can be decomposed into Fourier components which show a different behavior as a function of n. Many iterative solvers reduce the short-wave components of ε_n fairly fast, whereas they are very slow in eliminating the long-wave components. The multigrid method makes use of the fact that in order to eliminate the long-wave components, a coarse grid is sufficient. On a coarse grid the effort for obtaining the updated field Φ_{n+1} from Eq. (61) is reduced. In addition, the whole iteration scheme usually converges faster, thus further saving computational effort. Within a multigrid method a number of grids with different resolution are employed to reduce the different Fourier components of ε_n. In order to perform that task, a minimum number of numerical building blocks is necessary:

- An iterative solution method for linear algebraic systems which damps the short-wave components of the iteration error very fast and, after a few iterations, leaves predominantly long-wave components. The Gauss–Seidel method [85] could be chosen as a suitable solver in this context.
- A method for smoothing the residual obtained on the fine grid in order to compute the corresponding residual on the coarse grid. In the terminology of the multigrid method, this step is called *restriction*.
- A method for interpolating the update to the solution obtained on the coarse grid to the fine one. The interpolation step is denoted *prolongation*.

In one cycle of the multigrid method, first a few iterations are performed on the fine grid in order to obtain a comparatively smooth iteration error. After that the obtained residual is restricted to the coarse grid, where further iterations are performed in order to damp out the long-wave components of the solution error. Subsequently the coarse-grid solution is interpolated to the fine grid and the solution on the fine grid is updated.

In order to damp effectively the solution error on all length scales, it is advisable to work not just with two, but with a multitude of different grids. There are in principle two different strategies for directing the information flow between grids of different resolution [99]. One can take the point of view that one moves to a coarser grid as soon as the short-wavelength Fourier components have been damped on the finer grid and any further iteration would only effect a very slow reduction of long-wave components. Damping the long-wave components of the iteration error on a coarser grid is preferable owing to the reduced computational cost. A recursive implementation of such a strategy is depicted on the left side of Figure 2.16. The solution procedure starts with a few iterations on a grid with spacing h, then the solution is restricted to a grid with spacing $2h$ and the steps are repeated until the coarsest grid is reached. After that, the coarsest-grid solution is prolongated to a finer grid ($8h$), and the corrected solution obtained from the prolongation is taken as initialization for a few further iterations on the finer grid. The procedure is repeated until the finest grid is reached, on which the approximative solution of the problem is obtained.

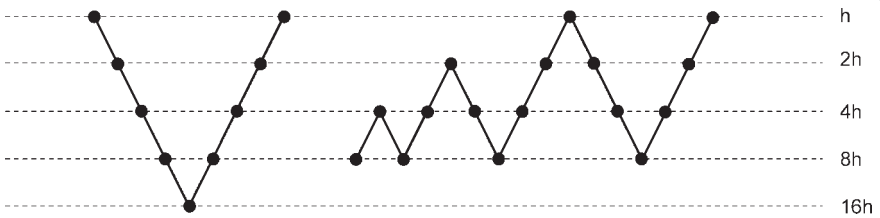

Figure 2.16 Two different schemes for the information flow between grids of different scale.

The other point of view concerning the information flow between different grids assumes that the iterations on a coarse grid provide an initial guess for the solution procedure on a fine grid. Correspondingly, one starts at the coarsest grid and successively moves on to finer grids. When implementing this idea and allowing for intermediate restrictions to coarser grids in order to damp the long-wave components of the iteration error, a scheme as depicted on the right side of Figure 2.16 is obtained.

Multigrid methods have proven to be powerful algorithms for the solution of linear algebraic equations. They are to be considered as a combination of different techniques allowing specific weaknesses of iterative solvers to be overcome. For this reason, most state-of-the-art commercial CFD solvers offer the multigrid capability.

2.4 Flow Distributions

In this and the following sections, the application of modeling and simulation techniques in the field of chemical micro process technology will be discussed. Several examples highlight the work that has already been done in this area and also the specific problems arising in the context of micro reactor and process design. Since the basic framework of numerical techniques was outlined in the previous section, in the following only specific models and special techniques allowing the corresponding problems to be solved efficiently will be discussed. In this context, not everything will rest on the fundaments of the FVM, but also other approaches, based on, e.g., finite-element or macro model approaches, play a role. As a discussion of the details of these numerical methods would be beyond the scope of this book, the reader is referred to the references given in the previous section for further information on these topics.

The focus of the examples given in this chapter is clearly on micro reactors for chemical processing in contrast to μ-TAS or Lab-Chip systems for bioanalytical applications. In the latter microfluidic systems, the fluidic requirements are somehow different from those in micro reactors. Typically, throughput plays only a minor role in μ-TAS systems, in contrast to micro reactors, where often the goal is to achieve a maximum molar flux per unit volume of a specific product. Moreover, flow control plays a much greater role in μ-TAS systems than in micro reactors. In

μ-TAS systems it is often required to transport fluid volumes in a very exact and highly synchronized way, and dosing and metering operations are of major importance. Whereas μ-TAS systems are mostly based on liquid flows, many micro reactors rely on gas flows or multiphase flows. According to this distinction, some of the effects which have been utilized to meet the specific requirements of μ-TAS systems will not be discussed here. Examples of such effects are electrophoresis, electroosmosis or liquid transport by electrowetting.

Owing to the specific microstructuring technology employed to build up micro reactors, the geometric shape of the flow domain is often different from that in macroscopic equipment. Whereas usually the elements for fluid transport such as pipes are of circular cross-section, the channels in micro reactors have a rectangular or trapezoidal cross-section. Depending on the specific microstructuring technology, tub-like grooves or close-to triangular shapes might also be obtained, especially when after microfabrication a catalyst layer is deposited on the channel walls. Furthermore, a characteristic feature that many micro reactors have in common is a comparatively wide flow distributor followed by a large number of parallel micro channels. In the following, the flow distributions in these characteristic geometries and methods to obtain approximate flow distributions in highly parallel flow domains will be discussed.

2.4.1 Flow in Rectangular Channels

For laminar flow in channels of rectangular cross-section, the velocity profile can be determined analytically. For this purpose, incompressible flow as described by Eq. (16) is assumed. The flow profile can be expressed in form of a series expansion (see [100] and references therein), which, however, is not always useful for practical applications where often only a fair approximation of the velocity field over the channel cross-section is needed. Purday [101] suggested an approximate solution of the form

$$u(x,y) = u_{\max}\left[1-\left(\frac{x}{a}\right)^{s}\right]\left[1-\left(\frac{y}{b}\right)^{r}\right] \tag{68}$$

for a rectangular channel oriented along the z-axis with a width $2a$ in the x-direction and a depth $2b$ in the y-direction, where u is the local flow velocity and u_{max} the maximum velocity. The exponents s and r depend on the aspect ratio b/a of the channel; the most common correlations can be looked up elsewhere [100]. Typically, Eq. (68) approximates the exact velocity profile with an accuracy of a few percent. Often, not the detailed velocity profile is of interest, but only the friction factor f which determines the pressure drop over a channel of a given length. The fanning friction factor is defined as

$$f = -\frac{\mathrm{d}p}{\mathrm{d}z}\frac{D_{\mathrm{h}}}{2\,\rho\,U^{2}}\,, \tag{69}$$

with dp/dz being the pressure gradient along the channel, ρ the density, D_h the hydraulic diameter and U the mean flow velocity. The hydraulic diameter is given by $4A/P$, with A being the cross-sectional area of the channel and P its perimeter. Shah and London [102] derived a comparatively simple expression for the friction factor in rectangular channels which deviates from the analytical solution by less than 0.05%:

$$f = \frac{24}{\mathrm{Re}}\left(1 - 1.3553\,\alpha + 1.9467\,\alpha^2 - 1.7012\,\alpha^3 + 0.9564\,\alpha^4 - 0.2537\,\alpha^5\right), \quad (70)$$

where α is the aspect ratio of the channel ($\alpha \leq 1$ by definition) and the length scale entering the Reynolds number Re is the hydraulic diameter.

Most expressions for the flow profile in rectangular channels assume that the flow is fully developed, i.e. that the flow velocity is oriented along the z-axis and does not change in streamwise direction. Close to the entrance of a channel this assumption is not valid, and the flow undergoes a development from an entrance distribution to a fully developed profile. Correspondingly, the pressure distribution deviates from that observed in a fully developed flow and expressions for the friction factor such as Eq. (70) are not valid in the entrance region. In order to determine the developing velocity distribution and friction factor, various approaches have been employed, such as analytical calculations based on a linearized inertia term, numerical solutions of the Navier–Stokes equation or experimental velocity and pressure measurements. An overview of the results was given by Hartnett and Kostic [100]. In general, the pressure drop per unit length of an entrance flow is higher than that of a fully developed flow. In order to compare entrance flow effects, a hydrodynamic entrance length L_{hy} can be defined which is the length necessary to achieve a centerline velocity equal to 99% of the fully developed value. Usually, a non-dimensional quantity is used, defined as

$$L_{hy}^{+} = \frac{L_{hy}}{D_h\,\mathrm{Re}}. \quad (71)$$

Depending on the aspect ratio of the channel, values between 0.01 and 0.1 are found for the non-dimensional entrance length [100]. From Eq. (71) it can be deduced, with L_{hy}^{+} being Re independent, that L_{hy} increases linearly with the hydraulic diameter and the Reynolds number.

2.4.2 Generalized Channel Cross-Sections

A number of authors have considered channel cross-sections other than rectangular [102–104]. Figure 2.17 shows some examples of cross-sections for which friction factors and Nusselt numbers were computed. In general, an analytical solution of the Navier–Stokes and the enthalpy equations in such channel geometries would be involved owing to the implementation of the wall boundary condition. For this reason, usually numerical methods are employed to study laminar flow and heat transfer in channels with arbitrary cross-sectional geometry.

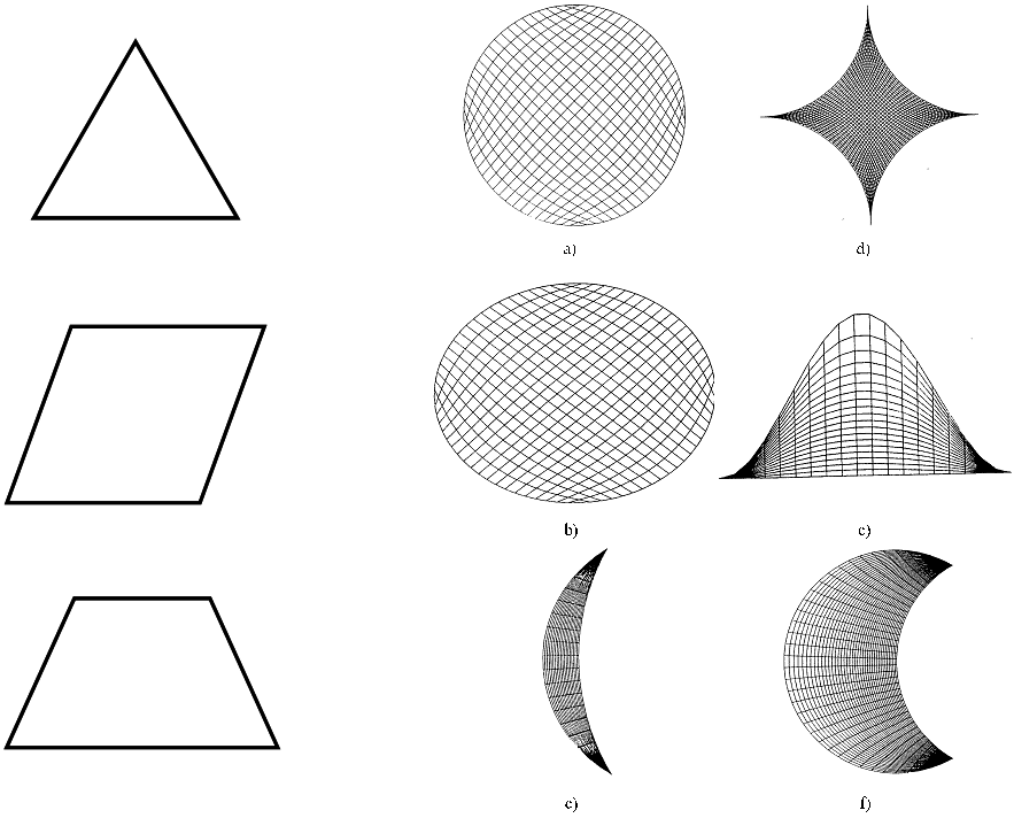

Figure 2.17 Channel cross-sections considered by Shah [103] (left) and by Richardson et al. [104] (right) in their numerical studies of laminar flows.

Shah [103] used a spectral method to compute the friction factors in ducts of triangular, rhombic and trapezoidal cross-section, among others. The results were given as tabulated values for different geometric parameters. Richardson et al. [104] considered the cross-sectional geometries which are shown on the right side of Figure 2.17 together with the computational grid. They used a finite-volume method to compute the velocity and the temperature field inside such channels and displayed their results in the form of an entropy generation rate going along with viscous friction.

2.4.3 Periodic and Curved Channel Geometries

Besides channels with different cross-sections, channels with specific periodic shapes were considered by several authors, mostly in the framework of 2-D simulations. Three different channel shapes having been studied are shown in

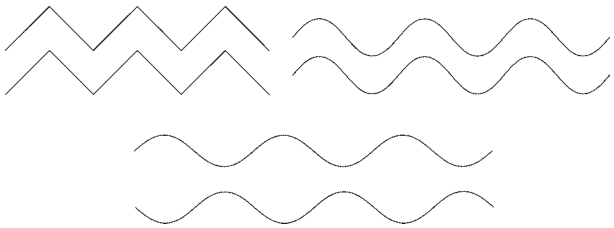

Figure 2.18 Different channel shapes for which flow distributions have been computed, a zigzag (upper left), a sinusoidally curved (upper right) and a converging–diverging channel (bottom).

Figure 2.18, a zigzag (upper left), a sinusoidally curved (upper right) and a converging–diverging channel (bottom). Asako and Faghri [105] computed velocity and temperature fields in zigzag channels based on the FVM for Reynolds numbers up to 1500. They found that above a specific Reynolds number depending on the geometry parameters, flow separation occurs, i.e. in the corners of the channel recirculation zones are being formed. Whereas the friction factor for straight channels displays a linear decrease as a function of Reynolds number, as is apparent from Eq. (70), the friction factor in zigzag channels becomes nearly independent of the Reynolds number for $Re > 1000$. Flow in sinusoidally curved channels for Reynolds numbers up to 500 was studied by Garg and Maji [106]. Again, a finite-volume discretization was used. For most of the parameter space explored, flow separation was not observed. However, for $Re = 500$ and a large enough sine-wave amplitude as compared with the period, there were some indications of recirculation zones forming in the recesses of the channel. Unfortunately, no attempt was made to compute friction factors.

Guzmán and Amon [107] studied flow in converging–diverging channels and paid special attention to the transition between laminar and turbulent flow. They used a spectral-element method where the flow domain is divided into macro-elements over which a set of polynomial test functions is defined. Their method allowed damping of small-scale fluctuations due to numerical viscosity to be suppressed and is thus well suited to study the transition from stationary to oscillatory and chaotic flow. The computed streamline patterns indicate a transition from a non-separated flow at low Reynolds numbers to a flow with recirculation zones within the recesses of the channel, occurring at comparatively small Reynolds numbers between 10 and 20. Streamline patterns for various Reynolds numbers are depicted in Figure 2.19. The phenomenology of flow distributions in such channel domains was found to be diverse. At low Reynolds numbers the flow is stationary, but at a Reynolds number of 150 oscillations begin to develop, with the vortices still being confined in the recesses. At $Re = 400$ the viscous forces are no longer strong enough to confine the vortices in the recesses and vortex ejection is observed. At even higher Reynolds numbers the flow becomes aperiodic and chaotic. Guzmán and Amon further analyzed the flow patterns using methods established in chaos theory based on, e.g., Poincaré sections, pseudo-phase space representations and Lyapunov exponents, and thereby provided a detailed flow map of the laminar-to-turbulent transition in converging–diverging channels.

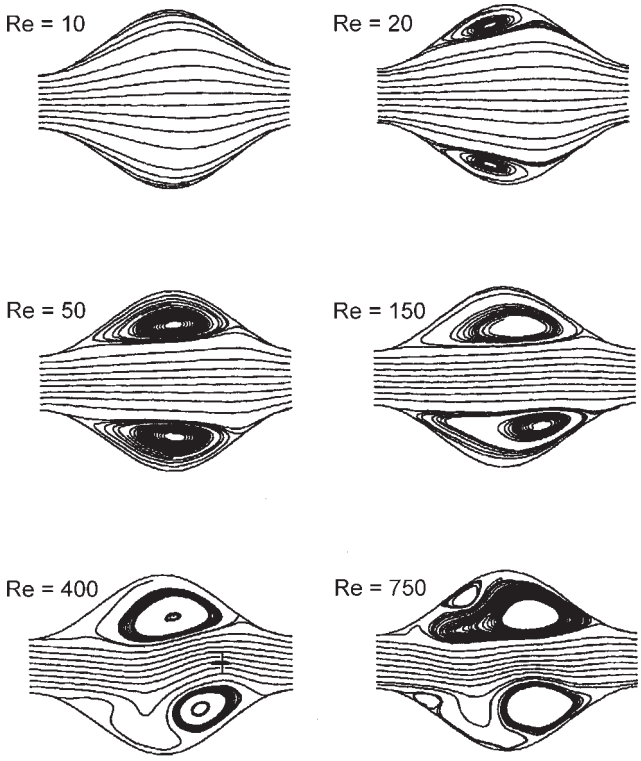

Figure 2.19 Streamline patterns in a converging–diverging channel for various Reynolds numbers, taken from [107].

In some cases, for example when large residence times are desired, comparatively long micro channels have to be integrated into a compact micro reaction device, a task which can only be achieved with curved channels. In addition, straight channels are often not suited for connecting a micro flow domain to the external world. One of the first theoretical studies on flow in curved channels was done by Dean [108, 109], who investigated the secondary flow perpendicular to the main flow direction induced by inertial forces using a perturbative analysis. The dimensionless group characterizing such transversal flows is the Dean number, defined as

$$K = \mathrm{Re}\sqrt{\frac{D_\mathrm{h}}{R}}\,, \tag{72}$$

where D_h is the hydraulic diameter and R the mean radius of curvature of the channel. The typical secondary flow pattern in curved channels is given by two counter-rotating vortices separated by the plane of curvature. The strength of these vortices increases with increasing Dean number. Originally, the studies of secondary flow in curved channels were performed for pipes of circular cross-section.

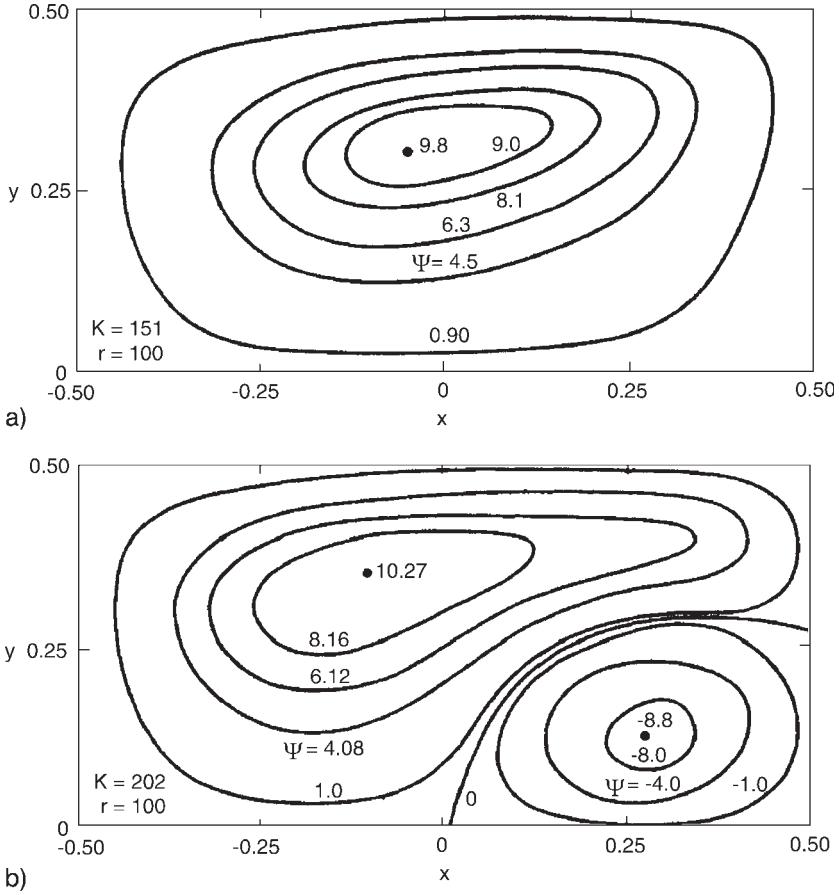

Figure 2.20 Streamline patterns of secondary flow in quadratic channels for $K = 151$ (above) and $K = 202$ (below), taken from [110]. Only the upper half of the channel cross-section is shown.

Of much greater relevance in micro reactors are rectangular channels, which were the subject of a study by Cheng et al. [110], among others. They solved the Navier–Stokes equation for channel cross-sections with an aspect ratio between 0.5 and 5 and Dean numbers between 5 and 715 using a finite-difference method. The vortex patterns obtained as a result of their computations are depicted in Figure 2.20 for two different Dean numbers.

As a result of the inertial forces exerted on the fluid elements due to the curvature of the channel, a pair of counter-rotating vortices transporting fluid perpendicular to the main flow direction is formed. When the Dean number is increased to values larger than 200, a second pair of vortices emerges close to the outer channel wall. In addition to the secondary flow patterns, Cheng et al. computed the axial velocity distribution and friction factors for different Reynolds and Dean numbers. Not surprisingly, the friction factor in curved channels was found to be larger than that in straight channels.

2.4.4 Multichannel Flow Domains

In chemical micro process technology, on the one hand it is important to guarantee well-defined and reproducible reaction conditions in micro channels, and on the other a high throughput should be achieved. For this purpose, the process fluid is guided through a large number of parallel micro channels, where heat exchange and/or chemical reactions occur. One of the characteristic problems in micro process technology is to distribute the incoming fluid equally over the micro channels. A fluid maldistribution would induce unequal residence times in different channels, with undesirable consequences for the product distribution of a chemical reaction being conducted inside the reactor. When a process with various competing side reactions and by-products is considered, the contact time of the process fluid in the reaction region should be as well defined as possible in order to maximize the selectivity of the process. However, it should be pointed out that not only the maldistribution of the fluid over a multitude of micro channels induces variations of the contact time, but also hydrodynamic dispersion of concentration tracers in the channels themselves. The corresponding effects will be discussed in a subsequent section devoted to mass transfer.

Various concepts for the equipartition of fluid over a multitude of micro channels have been developed. One concept relies on guiding the incoming fluid through a flow splitter with subsequent bifurcations [111]. The most widely used design is based on a comparatively wide inlet region leading into a multitude of narrow micro channels. A corresponding design, developed for methanol reforming, is shown in Figure 2.21. The figure shows the computational domain of the CFD model of the reactor, where use of reflection symmetry was made and only one quarter of the portion of the reactor to be considered was modeled. An inlet pipe leads to a flow distribution chamber connected with a multitude of micro channels. The essence of such designs is to be seen in the pressure barrier of the micro channels. The narrower the micro channels are, the higher will be the pressure

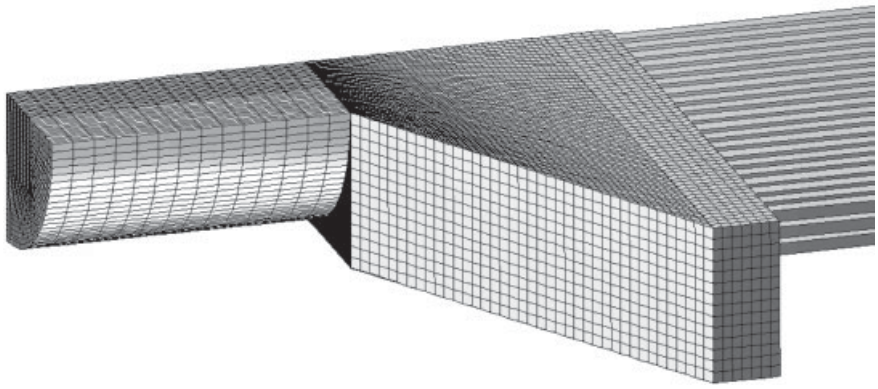

Figure 2.21 Computational domain of a multichannel reactor for methanol reforming.

drop in the channels themselves as compared with the pressure drop in the flow distribution chamber, and the more uniform the flow distribution will be.

Walter et al. studied the flow distribution in simple multichannel geometries by means of the finite-element method [112]. In order to reduce the computational effort, a 2-D model was set up to mimic the 3-D multichannel geometry. Even at a comparatively small Reynolds number of 30 they found recirculation zones in the flow distribution chamber and corresponding deviations from the mean flow rate inside the channels of about 20%. They also investigated the influence of contact time variation on a simple two-step reaction.

Also a simulation of the flow field in the methanol-reforming reactor of Figure 2.21 by means of the finite-volume method shows that recirculation zones are formed in the flow distribution chamber (see Figure 2.22). One of the goals of the work focused on the development of a micro reformer was to design the flow manifold in such a way that the volume flows in the different reaction channels are approximately the same [113]. In spite of the recirculation zones found, for the chosen design a flow variation of about 2% between different channels was predicted from the CFD simulations. In the application under study a washcoat cata-

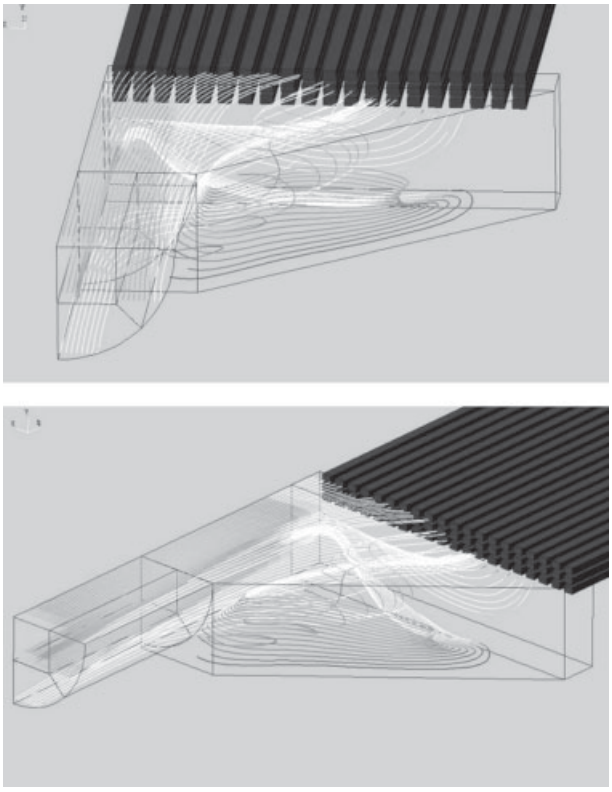

Figure 2.22 Streamlines in the flow distribution chamber of a multichannel reactor.

lyst layer is applied to the micro channels. The thickness variations of the catalyst layer are likely to play the leading role in the non-uniformities in flow distribution to be expected. Hence a flow manifold with intrinsic volume flow variations of a few percent over different reaction channels is usually satisfactory.

For the computation of the flow distribution in the methanol-reforming reactor, a reduced-order flow model for the micro channels was used. In such a model a fully developed flow profile as given by Eq. (68) is assumed, which means that entrance flow effects are neglected. This approximation is justified when the entrance length is small compared with the total length of the channel. A major advantage of a reduced-order flow model is the significant reduction of the degrees of freedom entering the simulation. Each micro channel is then only represented by a single degree of freedom which is the total volume flow, and a resolution of the flow domain by a computational grid is no longer required. In this way the simulation of microfluidic devices comprising a large number of channels becomes possible.

Another special feature allowing efficient simulation of flows entering from a flow-distribution chamber into a multitude of channels is the possibility to combine non-matching grids. Figure 2.23 displays an interface between a rectangular and a body-fitted grid. The center of the figure shows a projection of the two grids on to each other. A face of a rectangular grid cell overlaps with several faces of body-fitted grid cells, as depicted on the right. Domain decomposition methods with non-matching grids are an active research field of applied mathematics. In a specific class of methods the communication between different domains (i.e. different non-matching grids) is done via interfaces on which a space of shape functions is defined [114]. The solution of the full problem is then equivalent to the solution of an adjoint problem defined on the lower dimensional interface between the domains and the original problem in the different sub-domains. The solution of the adjoint equation defined on the interface provides the boundary conditions for the solution of the original transport equations within the sub-domains. Such methods were first developed in the framework of the finite-element approximation and were then extended to finite volumes [115]. The possibility of combining

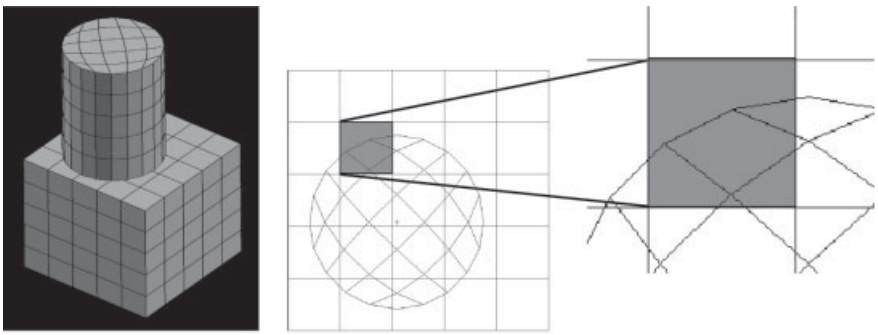

Figure 2.23 Arbitrary interface between a body-fitted and a rectangular grid.
A face of a rectangular-grid cell overlaps with several faces of body-fitted grid cells.

non-matching grids allows one to grid each sub-domain with the most appropriate mesh while paying little attention to the transition between different meshes. In this way it is possible to set up a computational domain of, e.g., a flow distribution chamber interfacing with a number of channels, without the need to define an unstructured grid.

Finite-volume grids with arbitrary interfaces in combination with reduced-order flow models for micro channels allow one to solve flow distribution problems in 3-D for which the standard approach of interface-matched grids and discretized channel cross-sections would be computationally too expensive. However, when the goal is to find designs with an optimum flow equipartition by tuning specific geometric parameters, even an approach based on arbitrary grid interfaces might lead to intolerable CPU times. An optimization usually requires doing a large number of evaluations of a corresponding cost function, which means that repeated computations of the flow distribution for specific geometries would be necessary. Apart from a few special cases, such optimizations are only possible with simplified models. Commenge et al. studied the flow distribution in multichannel micro reactors with the help of macro models [116]. The geometry they considered was a microstructured plate of a heat-exchanger stack developed at the Institute of Microtechnology Mainz. The plate together with arrows indicating the flow direction is shown on the left of Figure 2.24, and the right the model set up by Commenge et al. together with the geometric parameters is displayed. The model is based on the idea of subdividing the flow domain into a number of channel segments with rectangular cross-section over which the flow is distributed. Through the channel segments in the inlet zone the volume flows V_1, V_2, ..., V_{nc} are transported, where a part of the flow branches off into the actual micro channels of width W_c and depth e. For each of the channel segments a relationship between the pressure drop Δp and the average flow velocity u of the form

$$\Delta p = 32\, \lambda_{nc}\, \frac{\mu\, L\, u}{D_h^2} \tag{73}$$

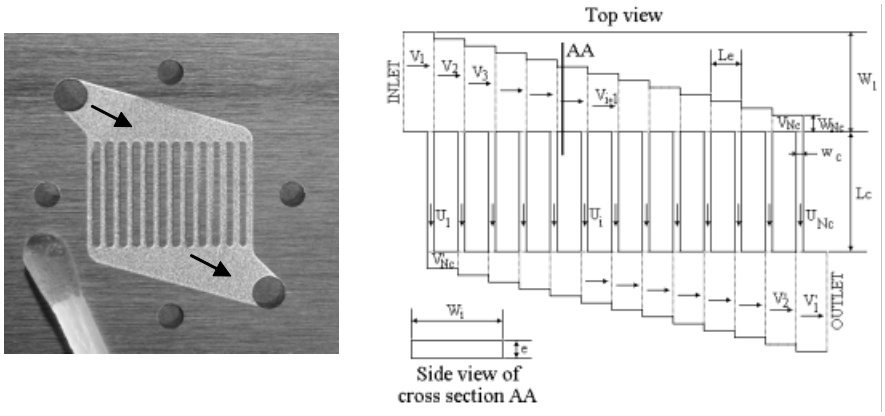

Figure 2.24 Geometry of the microstructured plates (left) and subdivision of the flow domain into channel segments (right) as considered in [116].

was used, where the hydraulic diameter is defined as

$$D_{\mathrm{h}} = \frac{2\,w\,e}{w + e}. \tag{74}$$

In these expressions, μ is the dynamic viscosity, L the length of the channel segment, w and e their width and depth and λ_{nc} a correction factor accounting for the non-circularity of the channels. Clearly, the above equations rely on the assumption of a hydrodynamically developed flow.

By means of the model depicted in Figure 2.24, Eqs. (73) and (74), it is possible to compute the flow distribution just by solving a comparatively low-dimensional system of linear algebraic equations. The problem resembles the task of computing the current distribution of an electric circuit. *A priori* it is not clear if the approximation to subdivide the flow domain in the described way is justified. In order to assess the quality of the chosen approximation, Commenge et al. [116] computed the flow field by means of the finite volume method. The results obtained suggest that, owing to the orientation of the isobars of the flow and the absence of recirculation loops, the chosen subdivision into channel segments is a reasonable simplification, at least for the geometry and the flow regime considered. The model allows one to study the flow distribution for a variety of different geometries with a minimum computational effort. In Figure 2.25 the results for different geometries of the inlet chamber are displayed in the form of volume flow as a function of channel number. Depending on the geometry of the inlet chamber, the flow distribution over the channels assumes a concave (left), flat (middle) or convex (right) shape. In order to determine optimized chamber geometries, a numerical optimization algorithm was used. The velocity differences between different channels obtained with such optimized geometries are < 0.1%.

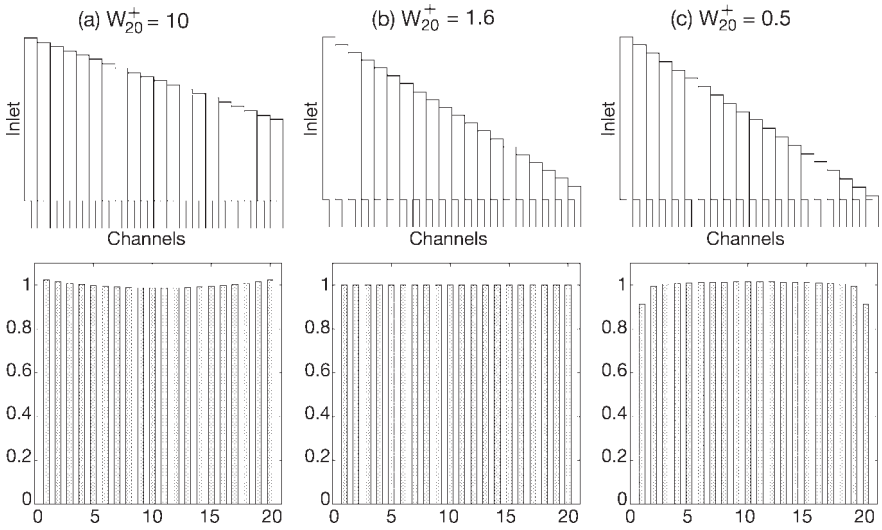

Figure 2.25 Normalized velocity distributions over 20 micro channels obtained by Commenge et al. [116] for a specific class of flow chamber geometries.

Although the strategy described above is a way to obtain effective, low-dimensional models for multichannel reactors in various cases, it clearly has its limitations. *A priori* the applicability of such models has to be carefully justified, and the simple approximations lose their validity when recirculation loops emerge. In geometries with hundreds of micro channels, another method can be utilized to compute the flow field. In a situation where the flow is distributed over a large number of parallel micro channels, the multitude of channels can be regarded as a porous medium. For porous media, effective, volume-averaged transport equations have been known for a long time (for an overview, see, e.g., [117]). In order to solve a flow distribution problem for a multichannel geometry, the flow domain can be split into several regions, one of them being the flow distribution chamber and another the region comprising the multitude of channels. In the flow distribution chamber, the ordinary transport equations are solved, whereas in the multichannel domain, the effective, volume-averaged description of the transport processes is used. A corresponding geometry is shown in Figure 2.26. The incoming flow distributes over a large number of channels with a width w_c separated by walls with a width $w - w_c$.

The most straightforward porous media model which can be used to describe the flow in the multichannel domain is the Darcy equation [117]. The Darcy equation represents a simple model used to relate the pressure drop and the flow velocity inside a porous medium. Applied to the geometry of Figure 2.26 it is written as

$$\frac{\mathrm{d}}{\mathrm{d}y}\langle p\rangle_f + \varepsilon\frac{\mu}{K}\langle u\rangle_f = 0\,, \tag{75}$$

with the porosity ε and the permeability K given as

$$\varepsilon = \frac{w_c}{w}, \quad K = \frac{\varepsilon\, w_c^2}{12}\,. \tag{76}$$

The flow velocity, pressure and dynamic viscosity are denoted u, p and μ and the symbol $\langle\ldots\rangle_f$ represents an average over the fluid phase. Kim et al. used an extended Darcy equation to model the flow distribution in a micro channel cooling device [118]. In general, the permeability K has to be regarded as a tensor quantity accounting for the anisotropy of the medium. Furthermore, the description can be generalized to include heat transfer effects in porous media. More details on transport processes in porous media will be presented in Section 2.9.

Compared with the use of arbitrary grid interfaces in combination with reduced-order flow models, the porous medium approach allows one to deal with an even larger multitude of micro channels. Furthermore, for comparatively simple geometries with only a limited number of channels, it represents a simple way to provide qualitative estimates of the flow distribution. However, as a coarse-grained description it does not reach the level of accuracy as reduced-order models. Compared with the macromodel approach as propagated by Commenge et al., the porous medium approach has a broader scope of applicability and can also be applied when recirculation zones appear in the flow distribution chamber. However, the macromodel approach is computationally less expensive and can ideally be used for optimization studies.

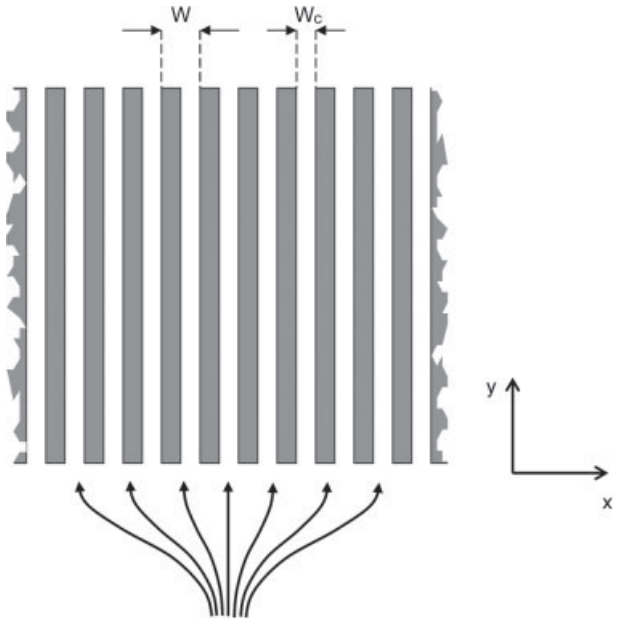

Figure 2.26 Multichannel geometry with channels and separating walls of uniform width.

2.5 Heat Transfer

Heat transfer phenomena belong to the key issues to be studied in micro reactors. Owing to the small thermal diffusion paths, micro reactors bear the potential to allow fast heat transfer and control of temperature distributions with very high accuracy. The excellent thermal performance of micro reactors is a key issue on which many processes of micro chemical engineering are based. Correspondingly, modeling and simulation of heat transfer phenomena and their reliable prediction are of paramount importance for process design. The simulation of temperature distributions in micro reactors often requires the solution of a conjugate heat transfer problem, i.e. the temperature fields in the fluid phase and in the solid wall material have to be computed. Owing to the microstructuring technologies used to fabricate micro reactors, the share of wall material in the total reactor volume is often higher than in conventional equipment. Hence solid heat conduction effects become important and usually have to be taken into account when the temperature field inside a reactor is to be computed.

2.5.1 Fundamental Equations of Heat Transport

The governing equation for the transport of heat contains convective and diffusive contributions. Inside the fluid phase, convective transport often dominates. Within

the solid walls the convective contribution is zero and heat is transported solely by conduction. The transport equation for heat, sometimes termed the energy or the enthalpy equation, can be written as (see, e.g., [119])

$$\rho\left(\frac{\partial e}{\partial t}+u_i\,\frac{\partial e}{\partial x_i}\right)+p\,\frac{\partial u_i}{\partial x_i}=\frac{\partial}{\partial x_i}\left(\lambda\,\frac{\partial T}{\partial x_i}\right)+\dot{q}_\mathrm{v}+\dot{q}\,, \tag{77}$$

where e denotes the thermal energy density, ρ the mass density, u_i the flow velocity, p pressure, T temperature, λ the thermal conductivity, $\dot{q}_\mathrm{v}$ the heat source due to viscous dissipation and $\dot{q}$ all other heat sources. In incompressible media the enthalpy equation simplifies to

$$\frac{\partial T}{\partial t}+u_i\,\frac{\partial T}{\partial x_i}=\frac{1}{\rho\,c_p}\left[\frac{\partial}{\partial x_i}\left(\lambda\,\frac{\partial T}{\partial x_i}\right)+\dot{q}_\mathrm{v}+\dot{q}\right], \tag{78}$$

where c_p denotes the specific heat at constant pressure. The viscous dissipation term describes the transformation of kinetic energy of the flow into heat and is given by

$$\dot{q}_\mathrm{v}=\frac{\mu}{2}\left(\frac{\partial u_i}{\partial x_k}+\frac{\partial u_k}{\partial x_i}\right)^2, \tag{79}$$

where μ denotes the dynamic viscosity. From the structure of the term it is obvious that viscous dissipation is primarily important in regions with large velocity gradients. Eq. (77) contains a number of contributions describing effects of different nature. The first term on the left-hand side describes the transport of heat via convection with the flow velocity u_i. The derivative $\partial u_\mathrm{i}/\partial x_\mathrm{i}$ in the second term on the left-hand side indicates compression or expansion of fluid volumes. Via such processes internal energy is transformed into potential energy and vice versa at a pressure level p. The first term on the right-hand side describes transport of heat via conduction. Finally, $\dot{q}$ contains all remaining source terms, such as heat generation via the absorbance of radiation. It should be emphasized that Eq. (77) is clearly not the most general form of an enthalpy equation. As an example, the thermal conductivity of a medium might be anisotropic, such that the scalar thermal conductivity λ would have to be replaced by a thermal conductivity tensor. Furthermore, inclusion of the cross-diffusion effects discussed in Section 2.2.1 would require adding terms proportional the gradient of chemical species concentration on the right-hand side.

The Navier–Stokes equation and the enthalpy equation are coupled in a complex way even in the case of incompressible fluids, since in general the viscosity is a function of temperature. There are, however, many situations in which such interdependencies can be neglected. As an example, the temperature variation in a microfluidic system might be so small that the viscosity can be assumed to be constant. In such cases the velocity field can be determined independently from the temperature field. When inserting the computed velocity field into Eq. (77) and expressing the energy density e by the temperature T, a linear equation in T is

obtained if the specific heat can be assumed to be temperature independent. The corresponding equation is much easier to solve than the non-linear Navier–Stokes equation.

2.5.2 Heat Transfer in Rectangular Channels

As stated in the previous section, a standard geometry of channels contained in microfluidic systems is a rectangular or close-to-rectangular cross-section. With a given velocity profile, the temperature field inside rectangular channels can often be determined analytically. However, it should be pointed out that the problem of determining a temperature profile in a channel geometry is much more multifaceted than the computation of a flow distribution. Whereas in most cases a zero-velocity boundary condition at the channel walls is prescribed for the flow, the wall-boundary conditions for the temperature field can be diverse. On the one hand, either a heat flux or a temperature can be prescribed. On the other hand, the thermal boundary conditions on the four walls of a rectangular channel might be different. Owing to this complexity, the solution for the temperature field itself is usually not reported. Rather, the Nusselt number, defined as

$$\mathrm{Nu} = \frac{k\, D_\mathrm{h}}{\lambda} \tag{80}$$

is determined, where D_h is the hydraulic diameter, λ the thermal conductivity and k the heat transfer coefficient measuring the transmitted thermal power per unit area divided by a characteristic temperature difference. The Nusselt number is a dimensionless quantity characterizing the efficiency of heat transfer. Similarly to the velocity field, the temperature field will assume an invariant profile far enough downstream from the channel entrance. However, owing to the continuous heat transfer from or to the channel walls, only the shape of the temperature distribution stays invariant, and the normalization changes. Close to the entrance of the channel, a thermally developing flow may be observed. A thermal entrance flow is *a priori* not related to a hydrodynamic entrance flow, i.e. a thermally developing flow might be observed even in regions where the flow is hydrodynamically developed and vice versa.

Hartnett and Kostic give an overview of the Nusselt numbers obtained for rectangular channels with various aspect ratios and various thermal boundary conditions [100]. Depending on the thermal boundary condition, the Nusselt number for thermally fully developed flow either increases or decreases when the aspect ratio is increased. When the Nusselt number for thermally developing and hydrodynamically developed flow is plotted as a function of position along the channel, a divergence is observed when the channel entrance is approached. This means that with decreasing distance to the channel entrance, increasing heat transfer efficiency is found. The same observation is made when a simultaneously (i.e. hydrodynamically and thermally) developing flow is considered. Analogous to hydrodynamically developing flows, a thermal entrance length L_th can be defined.

It is given as the duct length required for the Nusselt number to fall within a 5% interval of the fully developed value. Again, a dimensionless quantity

$$L_{\mathrm{th}}^{+} = \frac{L_{\mathrm{th}}}{D_{\mathrm{h}}\,\mathrm{Re}\,\mathrm{Pr}} \tag{81}$$

is used, where the Prandtl number Pr is the ratio of the momentum diffusivity (i.e. the kinematic viscosity) and the thermal diffusivity. The dimensionless thermal entrance length is a quantity depending only on the aspect ratio of the channel and the thermal boundary conditions. Hence L_{th} is a linear function of the hydraulic diameter, the Reynolds number and the Prandtl number.

2.5.3 Generalized Channel Cross-sections

In their studies of friction factors in channels with a number of different cross-sectional geometries, Shah [103] and Shah and London [102] also computed heat transfer properties. A few characteristic cross-sections for which Nusselt numbers were obtained are displayed on the left side of Figure 2.17. Their results include both the Nusselt numbers for fixed temperature and fixed heat flux wall boundary conditions and are given as tabulated values for different geometric parameters.

In addition to those more or less regular channel cross-sections, Richardson et al. [104] studied heat transfer in some more exotic channels as displayed on the right side of Figure 2.17. They numerically computed Nusselt numbers and expressed them as a dimensionless entropy generation rate, defined as

$$N_{\mathrm{S}} = \frac{\dot{S}}{\dot{m}\,c_{\mathrm{p}}}, \tag{82}$$

where $\dot{S}$ is the entropy generation per unit time and $\dot{m}$ the mass flow rate. In addition to the contribution from heat transfer between the fluid and the channel walls, $\dot{S}$ contains a contribution from viscous heating, which is discussed in Section 2.5.5.

2.5.4 Periodic Channel Geometries

Similarly as with the computation of friction factors, heat transfer has not only been studied in straight channels, but also in channels with specific periodic shapes. Asako and Faghri [105] computed Nusselt numbers in the zigzag channels shown in Figure 2.18 using a finite-volume approach in two dimensions. They found a significant increase in the Nusselt number as compared with a straight channel, i.e. a parallel-plates arrangement. For suitable geometry parameters, a Reynolds number in the range of 1000 and a Prandtl number of 8, a heat transfer enhancement factor of about 13 was computed. For a Prandtl number of 0.7 (corresponding to air) they compared the ratio of the heat fluxes achieved with the zigzag and

the straight channels at identical values of pumping power and pressure drop. It was found that the zigzag channel outperforms the straight channel by a factor of up to 6, i.e. for the same pumping power or pressure drop a considerably higher heat flux is achieved. This is an interesting result in view of the design of micro heat exchangers, where the goal is often to increase the heat flux while limiting the pressure drop.

Heat transfer in sinusoidally curved channels was studied by Garg and Maji [106]. Surprisingly, at a Reynolds number of 100 they obtained a value for the Nusselt number which is lower than the corresponding value in a parallel-plates channel. Such a suppression of heat transfer stands in contradiction to results recently obtained by Hardt et al. [120]. They considered sine-wave channel walls of comparatively large amplitude and solved the Navier–Stokes and the enthalpy equations using an FVM solver. The streamline patterns obtained from the simulations showed flow separation with recirculation zones developing in the recesses of the channel, as displayed on the left side of Figure 2.27. On the right side of the figure, the computed Nusselt number, being evaluated close to the exit of the computational domain, is plotted as a function of Reynolds number (note that in this case, in contrast to many other studies of 2-D channel geometries, the Reynolds number was based on the hydraulic diameter, which is twice the wall distance). The triangles represent the corresponding values obtained in parallel-plates geometry. The slight increase in the Nusselt number in the parallel-plates channel as a function of Reynolds number is due to the fact that in the entrance region of a channel, which increases with increasing Reynolds number, the Nusselt number is higher than for fully developed flow. For the sine-wave channel, a heat transfer enhancement increasing as a function of Reynolds number is observed. For the highest Reynolds number considered, heat transfer is enhanced by a factor of about 4.

In the articles cited above, the studies were restricted to steady-state flows, and steady-state solutions could be determined for the range of Reynolds numbers considered. Experimental work on flow and heat transfer in sinusoidally curved channels was conducted by Rush et al. [121]. Their results indicate heat-transfer enhancement and do not show evidence of a Nusselt number reduction in any range

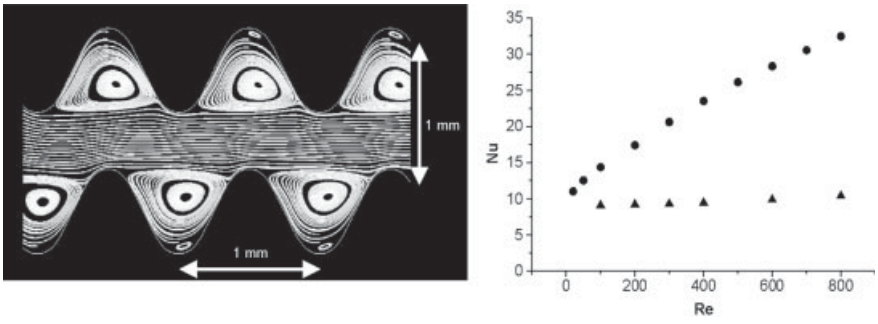

Figure 2.27 Streamline patterns in a channel with sinusoidal walls (left) and Nusselt number as a function of Reynolds number for the same channel (right), taken from [120]. For comparison, the triangles represent the Nusselt number obtained in parallel-plates geometry.

of Reynolds numbers. However, the flow patterns begin to exhibit some unsteady behavior for Reynolds numbers greater than about 200 in the geometry considered. Interestingly, oscillations were predominantly observed close to the exit of the channel and were found to move upstream when the Reynolds number was increased. Rush et al. attributed much of the heat-transfer enhancement found to the unsteady character of the flow.

The converging–diverging channel geometry for which Guzmán and Amon [107] computed flow fields was also considered by Wang and Vanka [122]. They computed the flow and temperature field in an elementary cell of the channel based on the finite-volume method using periodic boundary conditions. As far as the transition between a steady-state and an unsteady flow is concerned, they obtained similar results as Guzmán and Amon. At Reynolds numbers beyond the transition to the unsteady flow regime, the temperature field becomes complex. This is indicated in Figure 2.28, which shows the evolution of (normalized) temperature contour lines at a Reynolds number of 328. In order to quantify heat-transfer enhancement, the time-averaged Nusselt number was computed. The increase in Nusselt number compared with a straight channel was found to be significant and reached values as high as 7.54 at a Reynolds number of 520. However, the experimental results of Rush et al. [121], obtained for a comparable channel geometry, suggest that the assumption of periodic flow boundary conditions over one elementary cell of the channel might not be justified. The experiments show clear evidence of the flow pattern downstream in the channel being different from that one close to the channel entrance. Heat-transfer enhancement was also found in the experiments; however, the Nusselt numbers determined are significantly smaller than those predicted by Wang and Vanka.

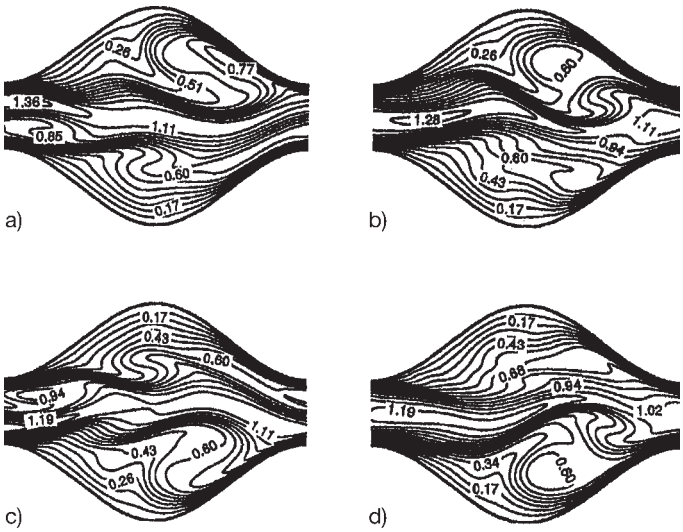

Figure 2.28 Evolution of the temperature field in the recesses of a converging–diverging channel, as obtained by Wang and Vanka [122].

2.5.5 Viscous Heating

In flow and heat transfer simulations in micro channels, the effect of viscous heating, described by Eq. (79), is often neglected. At fixed flow velocity, heat generation due to viscous heating scales as a power of $1/d^2$, where d is the diameter of the channel. Hence, when the channel diameter decreases, the importance of viscous heating grows rapidly and it might no longer be justified to neglect the corresponding effects. Sekulic et al. [123] and Richardson et al. [104] computed the entropy generation due to viscous heating for a variety of different channel cross-sections. As a second source of entropy besides viscous heating, the heat transfer from the fluid to the channel walls was considered. The transport equations for heat and momentum were solved using a finite-volume method on a body-fitted grid, with a fluid inlet temperature which was allowed to differ from the temperature of the channel walls. Typical results of these calculations for water as a fluid and a circular duct of 610 µm diameter are shown in Figure 2.29 as a function of Reynolds number. The labels on the different curves represent the different ratios of the inlet temperature and the temperature of the channel walls; for $\tau^* = 1.0$ both temperatures are equal. When τ^* increases, the heat transfer from the fluid to the channel walls begins to dominate the entropy generation. Heat transfer and viscous heating show a different behavior as a function of Reynolds number. When the Reynolds number increases, the residence time of the fluid in the channel the

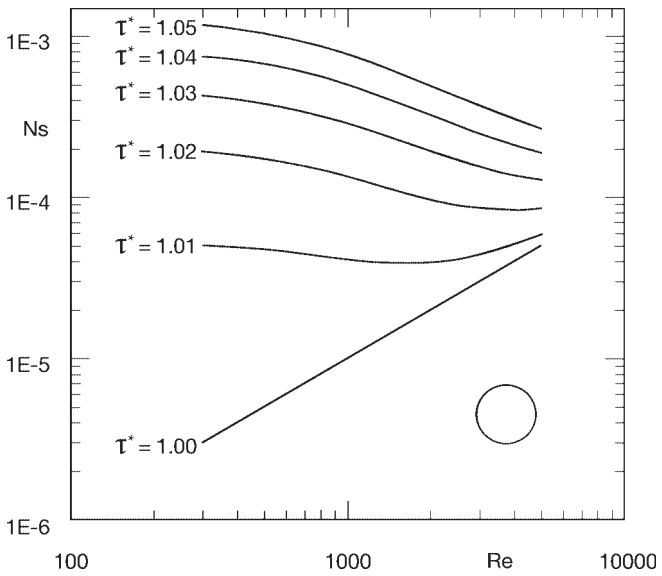

Figure 2.29 Dimensionless entropy generation rate as a function of Reynolds number for a circular channel of 610 µm diameter and different ratios of the fluid inlet temperature and the wall temperature, taken from [104].

entropy generation caused by the exchange of heat decreases. In contrast, an increasing Reynolds number is translated to an increasing flow velocity, which enhances the entropy generation due to viscous heating linearly. At a value of $\tau^* = 1.01$, the two effects add up in such a way that a minimum of the entropy generation curve is created within the range of Reynolds numbers considered. For Reynolds numbers in the region of 3000 the viscous heating effects become comparable in size to the entropy generation caused by the heat transfer from a fluid to channel walls with a temperature which is 1% lower.

Xu et al. [124] numerically computed the adiabatic temperature rise in a micro channel due to viscous heating and expressed their results by a correlation based on dimensionless groups. They introduced a dimensionless temperature rise $\Delta T^* = \Delta T / T_{\mathrm{ref}}$ with a reference temperature of 1 K. The correlation they found is given by

$$\Delta T^* = \frac{93.419\ \mathrm{Vi}\ \mathrm{Pr}^{-0.1}}{5.2086 + \mathrm{Vi}\ \mathrm{Pr}^{-0.1}}, \tag{83}$$

where Pr is the Prandtl number and Vi the viscous number, given by

$$\mathrm{Vi} = \frac{\mu\, \overline{u}\, L}{\rho\, c_{\mathrm{p}}\, T_{\mathrm{ref}}\, D^2}, \tag{84}$$

where $\overline{u}$ denotes the average velocity, L the length of the channel and D its diameter. Using this correlation, it can easily be judged when viscous heating has to be taken into consideration. The calculations of Sekulic et al., Richardson et al. and Xu et al. give an indication of how fast viscous heating effects become important when the channel dimension is reduced and may serve as a guideline for the design of microfluidic systems.

2.5.6 Micro Heat Exchangers

Micro heat exchangers represent a standard example of heat transfer in rectangular micro channels. Micro channel heat exchangers are used for rapid heat transfer between a hot and a cold fluid or, alternatively, as heat sinks for cooling devices. A schematic drawing of a counter-current heat exchanger is shown in Figure 2.30. A characteristic feature of such devices is the fact that the thickness of the wall material separating the channels is of the same order of magnitude as the channel depth itself. A micro heat exchanger might as well be operated in co-current mode, where the hot and the cold fluid flow in the same direction, or an arrangement with flow directions perpendicular to each other, the so-called cross-current mode, might be chosen.

Stief et al. [125] investigated the performance of counter-current micro heat exchangers, especially with respect to the wall conduction effects and the choice of

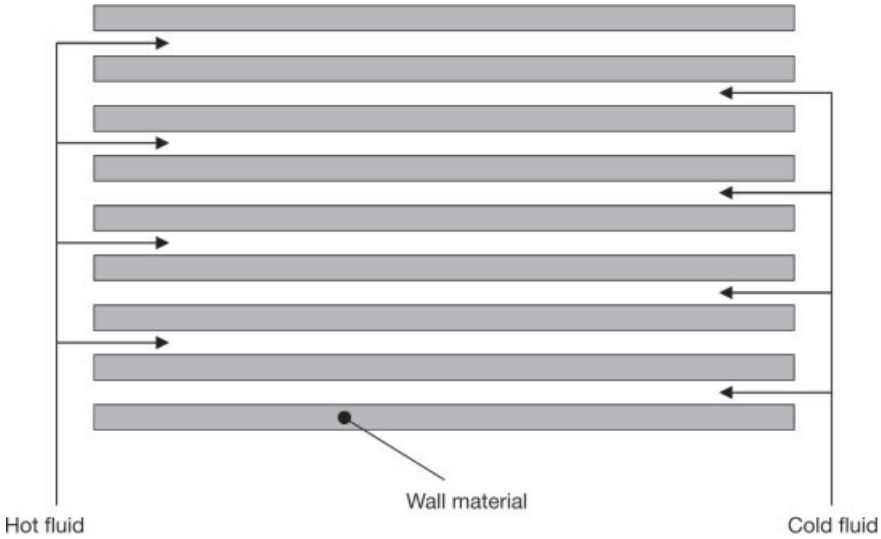

Figure 2.30 Schematic drawing of a counter-current micro heat exchanger.

the wall material. They considered a flow of nitrogen in channels with a length of 10 mm and a depth of 50 µm and separating walls of thickness between 125 and 500 µm. In the plane perpendicular to the flow direction, periodicity was assumed. In order to reduce the computational effort, the heat exchanger geometry was only discretized in the axial direction, i.e. in the direction of the flow. In the direction perpendicular to the flow a fixed heat transfer coefficient was used to describe the exchange of heat between the fluid and the channel walls. The resulting set of ordinary differential equations was solved by a special algorithm with adaptive step size control. When the thermal conductivity of the wall material is varied, characteristic temperature profiles for the channels with the hot and cold fluid and the channel wall are obtained, as displayed in Figure 2.31. For very small values of the

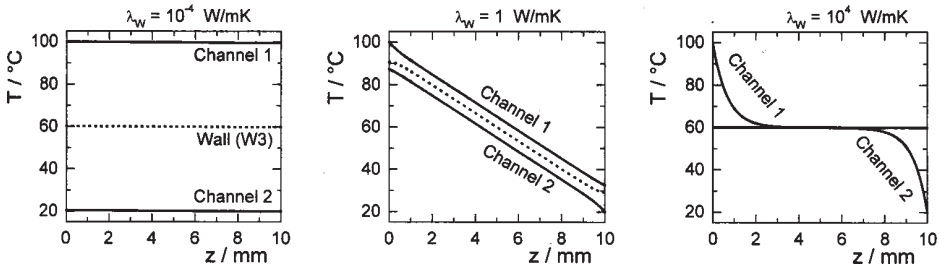

Figure 2.31 Characteristic temperature profiles in a counter-current micro heat exchanger for a very low (left), intermediate (middle) and very high (right) thermal conductivity of the wall material and equal volume flows inside the two channels, reproduced from [125].

thermal conductivity, no heat is exchanged and the temperatures stay approximately constant. At intermediate conductivities, almost linear temperature profiles are obtained, and at very high thermal conductivities the wall assumes a constant temperature and the temperature of the fluids changes rapidly in the entrance region of the channels.

A quantity characterizing the performance of a heat exchanger is the efficiency, which is the ratio of the transmitted heat and the maximum transmittable heat, given as

$$\varepsilon = \frac{T_{\text{in}}^{\text{hot}} - T_{\text{out}}^{\text{hot}}}{T_{\text{in}}^{\text{hot}} - T_{\text{in}}^{\text{cold}}} \tag{85}$$

in the case of equal volume flows two incompressible fluids. T_{in} and T_{out} denote the temperatures at the channel inlet and outlet, respectively. Stief et al. computed the heat exchanger efficiency for two characteristic geometries as a function of the wall thermal conductivity. A typical result for equal volume flows is displayed in Figure 2.32. At low conductivities almost no heat is transferred, as expected. At high conductivities the wall assumes a uniform temperature due to axial heat conduction and the device becomes indistinguishable from a co-current heat exchanger, which is limited to an efficiency of 50% at equal volume flows. At values around 1 W mK^{-1} the curve assumes a maximum, as axial heat conduction inside the walls is suppressed to a sufficient degree and transversal conduction to the opposite channels is still efficient. The position of the maximum is insensitive to the geometric parameters of the heat exchangers, Hence, in typical micro heat exchangers the use of low-conductivity materials such as glass or polymers is preferable, and the common stainless-steel materials are expected to reduce the efficiency.

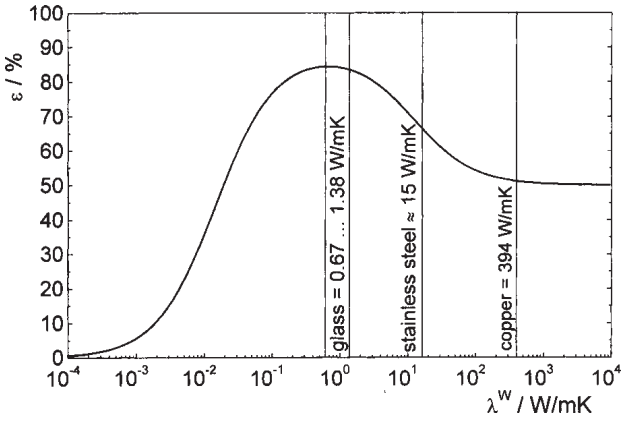

Figure 2.32 Heat exchanger efficiency as a function of the thermal conductivity of the wall, taken from [125].

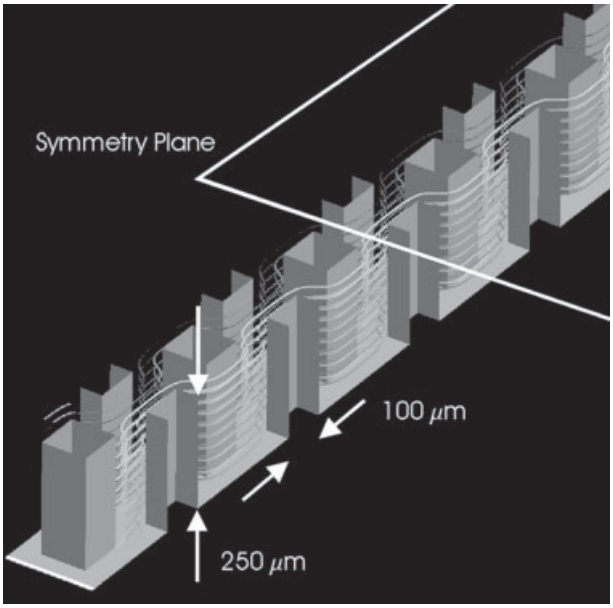

Figure 2.33 Heat exchanger micro channel with a checkerboard arrangement of micro fins, as considered by Hardt et al. [120].

Conventional heat exchangers rarely rely on simple flow geometries such as parallel channels [126]. Their design is usually optimized with regard to compactness, i.e. the transmitted heat flux per unit volume should be maximized. In general, flow in micro heat exchangers is laminar, in contrast to their macroscopic counterparts. Thus, owing to these different physical scenarios, the design concepts of conventional heat exchangers are not necessarily transferable to the world of micro process technology. Generic design features of heat exchangers are so-called fins, which are solid barriers introduced into the flow to remove heat from or introduce heat to the fluid efficiently. The problem of heat transfer enhancement in micro reactors by channels containing fins was studied by Hardt et al. [120]. They considered a channel with a checkerboard arrangement of micro fins of a cross-section of 100 µm × 100 µm, which is shown in Figure 2.33 together with the computed streamlines of the flow. Transversal to the main flow direction, the micro fin pattern is assumed to be repeated periodically *ad infinitum*.

The simulations of fluid flow and heat transfer in such microstructured geometries were carried out with an FVM solver. Air with an inlet temperature of 100 °C was considered as a fluid, and the channel walls were modeled as isothermal with a temperature of 0 °C. The streamline pattern is characterized by recirculation zones which develop behind the fins at comparatively high Reynolds numbers. The results of the heat transfer simulations are summarized in Figure 2.34, which shows the Nusselt number as a function of Reynolds number. For

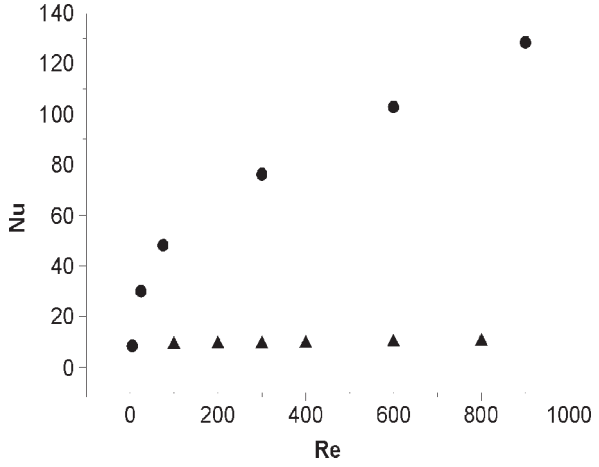

Figure 2.34 Nusselt number as a function of Reynolds number for a channel with a checkerboard arrangement of micro fins, taken from [120]. The triangles represent the Nusselt number obtained in a parallel-plates geometry.

comparison, the triangles represent the Nusselt number computed for channels of the same length as in the computational model, but with simple parallel-plates channel walls. The checkerboard arrangement of micro fins shows a significant increase in the Nusselt number as a function of Reynolds number.

The checkerboard micro fin arrangement with Nusselt numbers above 100 promises to allow a very high heat flux per unit volume. As the Nusselt number is a dimensionless measure of the heat flux per unit area, there is an additional increase in the total heat flux by the increase in surface area as compared with simple parallel-plates channel geometry. The increase in the Nusselt number in the micro fin geometry can be explained as a continuous entrance flow effect. As outlined previously, in the entrance region of a channel significantly higher Nusselt numbers are found than in downstream regions where the flow is fully developed. By the staggered arrangement of the micro fins shown in Figure 2.33 the flow is continuously forced to enter into barriers formed by two opposite micro fins and never reaches the equivalent of a developed state. However, the price to pay for the very fast heat transfer in the micro fin arrangement is a significant increase in the pressure drop in comparison with Poiseuille flow.

In order to examine the trade-off between heat exchange and pressure drop more closely, Drese and Hardt [127] studied micro fins of varying geometry. They chose a diamond-shaped fin cross-section as displayed on the left of Figure 2.35 and varied the fin length and the total fin length, while the fin width and the channel width were fixed to 50 μm. The goal was to identify geometries allowing for a maximum heat exchange for a given pressure drop. As a local dimensionless quantity which may serve as an indicator for such an efficiency figure, they identified the

ratio of the Nusselt and the Poiseuille number. The Poiseuille number is the ratio of the friction factor as defined in Eq. (69) and the Reynolds number. In order to determine optimized fin geometries, CFD simulations for flow of air and constant-temperature wall boundary conditions were performed for the staggered fin arrangement shown in Figure 2.35. The results as a function of mass flow per unit area are displayed below. The curves are distinguished by the different total fin length considered. Apparently, the ratio of Nusselt and Poiseuille numbers assumes distinctively different values for different fin geometries. For relatively elongated fins (200 µm total fin length), the ratio of Nusselt and Poiseuille numbers assumes favorable values above 0.4, thus indicating high heat transfer per unit pressure drop. For short fins, dead water areas or recirculation zones behind the fins give rise to a less favorable ratio of heat transfer to pressure drop. Hence efficient micro heat exchangers with low pressure drop may be designed by utilizing channel geometries with a staggered arrangement of comparatively long, diamond-shaped fins which suppress the formation of dead water areas and recirculation zones.

When a large number of parallel heat exchanger channels are considered, the problem of computing the temperature distribution inside the channels and the channel walls becomes involved, similar to the flow distribution problem discussed

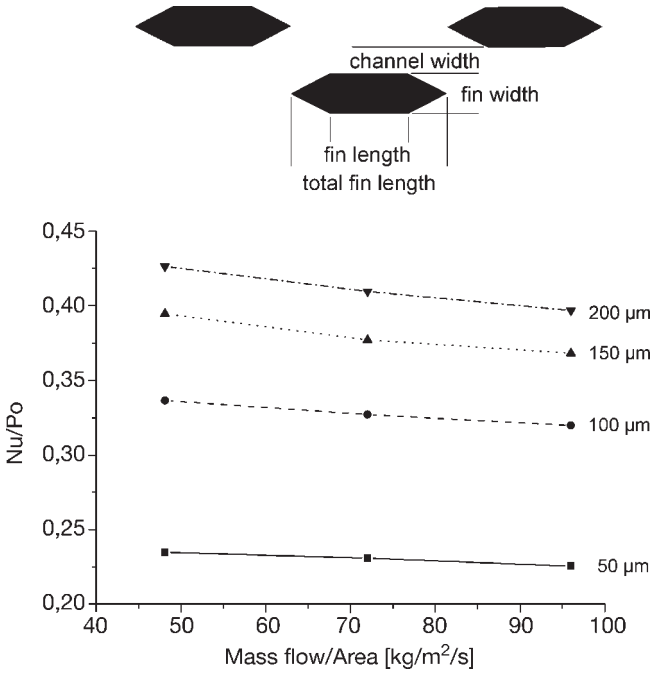

Figure 2.35 Cross-section through a staggered arrangement of micro fins designed for heat transfer enhancement in a micro channel (above) and ratio of Nusselt and Poiseuille numbers as a function of air flow per unit area for different total fin lengths (below), taken from [127].

in Section 2.4.4, and simplified models are needed. In such a case the use of the method of reduced-order flow models is not as straightforward as in the case of a pure flow distribution problem, owing to thermal cross talk between the different channels. Similarly, porous media models describing heat transfer in the multichannel domain are involved, as a temperature gradient orthogonal to the direction of flow induces a heat flux with components in the flow direction as well as orthogonal to it.

For simplicity, consider an incompressible medium flowing through the multichannel domain depicted in Figure 2.36. In a number of practical applications the heat flux in the x-direction will be very small compared with that in the y-direction. Then the volume-averaged enthalpy equation for the solid walls can be written as

$$\lambda_{s,\mathrm{eff}} \frac{\partial^2 \langle T \rangle_s}{\partial y^2} = \alpha\, a_{\mathrm{spec}} \left(\langle T \rangle_s - \langle T \rangle_f \right), \tag{86}$$

where $\langle ... \rangle_s$ represents a volume average over solid regions and $\lambda_{s,\mathrm{eff}}$ denotes the effective thermal conductivity of the solid matrix, T the temperature, α the heat transfer coefficient between the fluid and the solid and a_{spec} the internal surface area per unit volume of the multichannel domain. A corresponding averaging volume, embracing a number of channel and wall segments, is shown in Figure 2.36. The volume-averaged enthalpy equation for the fluid domain can be expressed as

$$\lambda_{f,\mathrm{eff}} \frac{\partial^2 \langle T \rangle_f}{\partial y^2} - \varepsilon\, \rho_f\, c_f\, \langle u \rangle_f \frac{\partial \langle T \rangle_f}{\partial y} = \alpha\, a_{\mathrm{spec}} \left(\langle T \rangle_f - \langle T \rangle_s \right), \tag{87}$$

where $\lambda_{f,\mathrm{eff}}$ denotes the effective thermal conductivity of the fluid domain, ε the porosity and ρ_f, c_f the fluid density and heat capacity, respectively. The volume-averaged fluid velocity $\langle u \rangle_f$ can be determined by solving Eq. (70) and, optionally, the momentum equation for the region upstream of the multichannel domain. The effective thermal conductivities in both regions are expressed as

$$\lambda_{s,\mathrm{eff}} = (1 - \varepsilon)\, \lambda_s\,, \quad \lambda_{f,\mathrm{eff}} = \varepsilon\, \lambda_f\,, \tag{88}$$

where λ_s and λ_f are the solid and fluid thermal conductivity, respectively.

Effectively, Eqs. (86) and (87) describe two interpenetrating continua which are thermally coupled. The value of the heat transfer coefficient α depends on the specific shape of the channels considered; suitable correlations have been determined for circular or for rectangular channels [100]. In general, the temperature fields obtained from Eqs. (86) and (87) for the solid and the fluid phases are different, in contrast to the assumptions made in most other models for heat transfer in porous media [117]. Kim et al. [118] have used a model similar to that described here to compute the temperature distribution in a micro channel heat sink. They considered various values of the channel width (expressed in dimensionless form as the Darcy number) and various ratios of the solid and fluid thermal conductivity and determined the regimes where major deviations of the fluid temperature from the solid temperature are found.

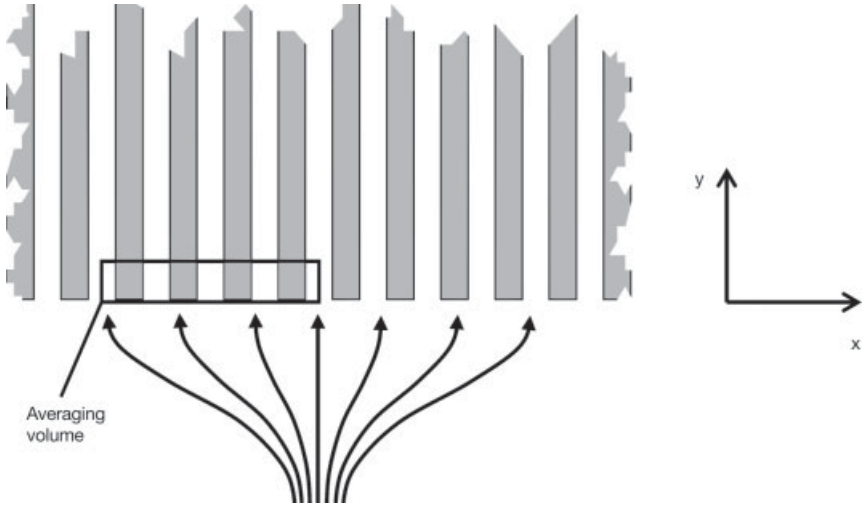

Figure 2.36 Multichannel flow domain with typical averaging volume for obtaining volume-averaged enthalpy equations.

2.5.7 Thermal Optimization of Micro reactors

One of the most prominent application areas of modeling and simulation techniques in chemical micro process technology is the design optimization of micro reactors. In this context, thermal problems are often comparatively easy to solve, as the transport equation for heat is linear in temperature and in various cases the flow field is influenced by the temperature field to only a very small degree and can be assumed as given. An optimization based solely on variations of the temperature distribution was demonstrated by Quiram et al. [128]. They investigated thermal issues of the T micro reactor developed at MIT for gas-phase reactions. The name 'T micro reactor' stems from the design with two feed channels and a reaction channel forming a T-shaped geometry. The temperature in the reaction channel can be controlled by a platinum heating meander integrated on the membrane sealing the channel.

For the computation of the velocity and the temperature field inside the reactor, a stabilized FEM method was used. Within the stabilized FEM method, numerical parameters are introduced to overcome instability problems frequently occurring for convection-dominated problems [129]. The same method, in combination with a special procedure to deal with highly non-linear sets of algebraic equations, was employed subsequently to compute the species concentration obtained via chemical reactions occurring in the reaction channel. By computing the temperature distribution in the reaction channel, Quiram et al. [130] were able to show that the initially proposed heater configuration produces a non-uniform temperature profile. By varying the geometry of the platinum heaters, a significantly flatter tem-

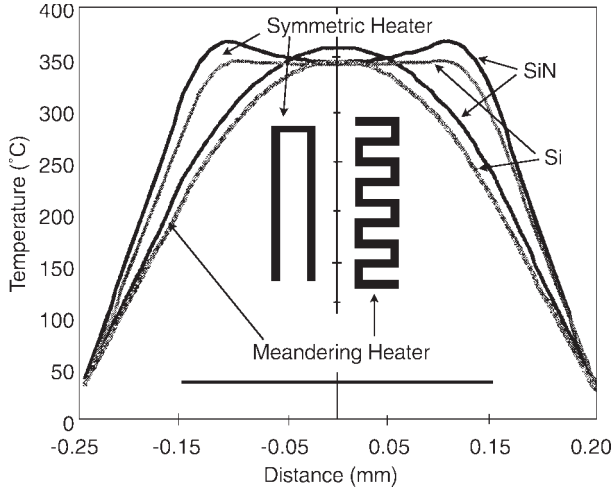

Figure 2.37 Temperature profiles across the membrane covering the reaction channel of the T micro reactor for a silicon and a silicon nitride membrane and two different heater designs, as discussed by Quiram et al. [128].

perature profile could be obtained. The obtained temperature profiles over the width of the reaction channel are displayed in Figure 2.37 for two different materials covering the channel. Attached to the cover membrane is a platinum heater, where one version thereof spans a considerable section of the channel width and the other version consists of strips located in both halves of the channel. The version with two heating strips apparently produces temperature profiles which qualify better to carry out reactions at a uniform temperature level.

2.6 Mass Transfer and Mixing

Similarly to heat transfer, fast mass transfer is one of the key aspects of micro reactors. Again, owing to the short diffusion paths, micro reactors permit a rapid mass transfer and a uniform solute concentration within the flow domain. Good control of reactant concentration throughout the whole reactor volume is a prerequisite for highly selective chemical reactions and helps to avoid hazardous operation regimes. In addition, overcoming mass transfer limitations by rapid mixing allows the exploitation of the rapid intrinsic kinetics of chemical reactions and allows a higher yield and conversion. However, when dealing with liquid-phase reactions, fast mixing remains a challenge even at length scales of 100 μm or less owing to the small diffusion constants in liquids.